Silver Nanoparticle Monolayers for Plasmonics and Surface-Enhanced Raman Spectroscopy

by

Rui Xiu He

A thesis

presented to the University of Waterloo

in fulfillment of the

thesis requirement for the degree

Master of Applied Science

in

Mechanical Engineering (Nanotechnology)

Waterloo, Ontario, Canada, 2016

Author's Declaration

I hereby declare that I am the sole author of this thesis. This is a true copy of the thesis, including any required final revisions, as accepted by my examiners.

I understand that my thesis may be made electronically available to the public.

Abstract

Silver nanoparticle monolayers are plasmonic surfaces which primarily find use as a highly sensitive substrate for surface enhanced Raman spectroscopy (SERS), and are also found in thin film solar cells. This thesis describes the development of silver nanoparticle monolayers for the trace detection of the dye molecule rhodamine 6G through the SERS effect, and studies the effect of plasmonic manipulation on SERS sensitivity. Plasmonic manipulation of the monolayer is performed by a pre-fabrication scheme and post-fabrication treatment through particle size tuning and thermal treatment respectively. The changes in the localized surface plasmon resonance (LSPR) are correlated with the observed morphological changes, and the resultant SERS sensitivity is evaluated. It is found that increasing particle size up to 65nm increases the signal intensity, despite the lowering of surface density. This is explained by a rapid increase in the SERS enhancement factor (EF), found using finite element modelling of the LSPR. Thermal treatment is found to decrease signal intensity, but provide the benefit of surface cleaning at 400°C. This leads to some signal recovery, but most importantly opens chemical pathways for surface modification. Both methods are shown to have a predictable effect on the LSPR, allowing for optimization of solar cell applications.

Acknowledgements

First and foremost, I thank my supervisor, Professor Norman Zhou, for the research opportunity, and his continual advice and support throughout all my research. My personal and professional growth under his supervision was tremendous, and I consider all the time spent in his group both valuable and rewarding.

I also have deep gratitude for my mentors and colleagues Peng Peng and Robert Liang for their constant guidance, assistance, and overall presence in the lab. I'd like to give special recognition to my other colleagues Ehsan Marzbanrad, Paula Russo, Ming Xiao, and Joyce Koo for all the support work, little pieces of advice, guidance, and insight given along the way.

I would also like to acknowledge the various professors, staff, and individuals who tend instrumentation and provide various supporting services, without which research would be the opposite of streamlined. In particular, I'd like to thank Professor Ting Tsui and his student Brandon Seo for scanning electron microscopy, and Richard Barber for absorption and Raman spectroscopy, and Debbie Collins for putting up with my continuous requests.

Table of Contents

List of Figures

List of Tables

List of Abbreviations

AEF	Analytical enhancement factor
APTES	(3-aminopropyl)triethoxysilane
EBL	Electron beam lithography
EF	Enhancement factor
LSPR	Localized surface plasmon resonance
MEF	Metal enhanced fluorescence
NIR	Near infrared
NP	Nanoparticle
PDMS	Poly(dimethylsiloxane)
PVP	Polyvinylpyrrolidone
R6G	Rhodamine 6G
SERS	Surface enhanced Raman spectroscopy
SEM	Scanning electron microscopy
SMEF	Single molecule enhancement factor
SPR	Surface plasmon resonance
TSC	Trisodium citrate

Chapter 1: Introduction

1.1 Overview

Silver nanoparticles are submicron sized particles of silver with dimensions typically ranging from 1nm to 100nm. Nanosilver has been produced for over a century, and possesses a diverse range of practical applications including in pigments, photography, and catalysis[1]. The last two decades have sparked a renewed interest in silver nanoparticles following the emergence of the field of plasmonics, as well as the advancement of nanoscale characterization techniques. As a result, silver nanoparticles have found many modern applications in chemistry, medicine, and engineering. Silver nanoparticles exhibit are antimicrobial, a property which is used in textiles[2] and medicine[3]. They are often used in catalysis for their high surface energy[4,5]. They are used as conductive paths in electronic inks[6] and as fillers for conductive pastes[7]. In addition, metal nanoparticles exhibit the localized surface plasmon resonance (LSPR) phenomenon, which is applied towards photocatalysis[8], plasmonic solar cells[9,10], and sensing as a biochemical label[11,12], in metal enhanced fluorescence (MEF)[13], and in surface enhanced Raman spectroscopy (SERS)[14,15].

The LSPR refers to the electromagnetically driven oscillation of conduction electrons across the bulk of a nanoparticle. This oscillation is resonant at visible wavelengths for silver nanoparticles, and depends on the geometry of the nanoparticle being excited. Generally, larger dimensions correspond to longer resonant wavelengths, and resonances correspond to the geometric symmetries present in the nanoparticle[16]. The LSPR causes extremely high local electromagnetic field enhancements at the nanoparticle surface, which drives and amplifies light irradiating and originating from the nanoparticle surface. This is responsible for the electromagnetic enhancement of Raman and fluorescent photons in SERS and MEF. Silver nanoparticle monolayers are LSPR active coatings which are primarily used as SERS substrates[17–19], but are also found in thin film solar cells as light trapping layers[9], or for plasmon enhanced charge carrier generation[10]. Monolayers are prepared via colloidal self-assembly on a polyelectrolyte supporting layer, which is a low cost and scalable approach

requiring no specialized equipment beyond standard chemistry apparatus. This bottom-up fabrication method is capable of producing nanostructures and junctions much smaller than top-down lithographic approaches, and results in highly sensitive substrates capable of single molecule detection[20,21].

Many research papers demonstrate the fabrication of silver nanoparticle monolayers through self-assembly, and their application in SERS[18–23]. Most of these authors independently develop their nanoparticles and substrates using various synthesis methods and immobilizing polyelectrolytes. While the prevalence of experimental evidence verifies the practicality of such substrates, fundamental studies on monolayer formation and the dependence of SERS activity on various substrate properties is an ongoing field of research. The Van Duyne research group has led several important fundamental studies on SERS including the dependence of excitation wavelength[24] and LSPR strength[25] on the EF. These studies showed that the greatest SERS signals can be achieved when the substrate LSPR, the wavelength of excitation, and the Raman band of the analyte molecule are all selected to work in harmony. This opens up the possibility of engineering the LSPR of substrates to optimize for a given Raman laser setup and analyte molecule.

This research project uses the self-assembly method to produce silver nanoparticle monolayers for use as SERS substrates, and explores two methods of LSPR manipulation: a pre-fabrication method by particle size tuning, and a post-fabrication heat treatment. The fabrication of such substrates is described in detail, and their SERS performance is evaluated using rhodamine 6G (R6G) as the target analyte molecule. Single molecule sensitivity to R6G is demonstrated. Particle size tuning is achieved at the synthesis, and thermal treatment is performed in a tube furnace from 150°C to 450°C. Changes in microstructure are characterized and correlated with the SERS performance and LSPR response. Finally, design implications for optimizing silver nanoparticle monolayers towards SERS and other applications is discussed.

1.2 Research Objectives

The main objective of this research is to develop a SERS sensor platform for the detection of trace amounts of biomolecules, and perform scientific studies on the sensor. Self-assembled

silver nanoparticle monolayers are a low cost SERS platform with a scalable fabrication. While several authors have studied such substrates in the past, this work describes the first successful replication of this type of SERS sensor our laboratory, and demonstrates single molecule detection using rhodamine 6G. In addition, the fundamental science of these types of substrates is a current topic of research, and studies were performed on the effect of nanoparticle size and heat treatment on the substrate optical properties and SERS performance. The goal of these studies was to experimentally correlate the behavior of the morphology, LSPR profile, and SERS performance to guide the optimization of this SERS platform in future applications. Specifically, the objectives of the work are:

1. Develop a procedure for the fabrication of silver nanoparticle monolayers
    - Achieve a monodisperse particle synthesis and uniform monolayer
    - Study the monolayer formation kinetics
2. Evaluate silver nanoparticle monolayers as SERS substrates
    - Determine SERS enhancement factor, and lower detection limit with a chosen target analyte
3. Perform plasmonic manipulation on the substrates and study the effect on SERS
    - Achieve syntheses of different particle sizes
    - Perform thermal treatment
    - Determine SERS enhancement factor using modified substrates
    - Correlate changes in morphology, LSPR, and SERS

1.2 Thesis Outline

This thesis contains one chapter of literature review, two chapters of experimental research, and a final chapter presenting the conclusions and future outlook of this work. Chapter 1 is an introduction to the thesis, explaining the motivation behind the work and the objectives of the work.

Chapter 2 contains a literature review, intended to provide a background understanding of the SERS effect, and outline the current state of SERS substrate technology.

Chapter 3 describes the development of a silver nanoparticle monolayer, and demonstrates its application towards SERS.

Chapter 4 consists of a study performed on silver nanoparticle monolayers to physically alter the monolayer structure to affect the LSPR, and correlate the changes observed with SERS performance.

Chapter 5 summarizes the conclusions drawn from this work and presents recommendations for future work on this material.

Chapter 2: Literature Review

2.1 Summary

The advent of modern nanoscale fabrication and characterization methods has spurned interest in the study of plasmonic nanostructures. These are materials which exhibit unique behavior due to their nanoscaled size, particularly in their interaction with light. At the heart of plasmonics is the surface plasmon resonance, which is the collective motion of conduction electron stimulated by light at a resonant frequency. The most promising technology to emerge out of plasmonics is surface enhanced Raman spectroscopy, in which the Raman signal intensity of an analyte molecule may be enhanced billionfold by surface plasmons. This has led to a technological arms race to develop SERS substrates for biomolecular detection assays, and has sprung many branching technologies based on the SERS effect. Silver nanoparticle monolayers present many fabrication advantages over their more engineered competitors, and are therefore a current topic of research. In this review, an introduction to the SERS concept, and an overview of SERS substrate technologies is given, intended to give the reader an idea of the current state of substrate development.

2.2 Introduction to Plasmonics

The field of plasmonics is an emerging branch of nanophotonics that studies the way metal nanostructures act as antennas to convert light into localized electric fields. In plasmonics, incoming light interacts with the free electrons in a metal to drive their oscillation, and the resultant excited electron cloud is referred to as a plasmon[26]. Plasmons are sensitive to the metal material properties, the local dielectric environment, and the wavelength of incident light[27]. Plasmons come in two flavors: surface plasmon polaritons (propagating plasmon), and localized surface plasmons[27]. The former is a surface effect which occurs when the planar dimension of the irradiate surface exceeds the wavelength of light, while the latter only occurs in isolated nanostructures where the wavelength of light is greater than the size of the nanostructure[26]. The two types of plasmons are illustrated in figure 1.

Surface plasmon polaritons occur when incident light couples to oscillation modes of free electrons at a metal surface, and propagate along the metal dielectric interface, travelling distances up hundreds of microns away from the initial excitation site[27]. These can be used to probe changes in the refractive index of thin films using reflectivity measurements, and enable imaging of antibody-antigen, DNA-DNA, and DNA-protein interactions in real time[28]. The resonance of these types of plasmons is called surface plasmon resonance (SPR). The localized surface plasmon resonance (LSPR) refers to the collective oscillation of conduction electrons confined to an individual nanoparticle, driven by a resonant frequency of light[27]. This phenomenon occurs in nanoparticles 10nm to 200nm in size[29], and results in amplification of the electric field **E** at the surface of the nanoparticle such that $|\mathbf{E}|^2$ can be up to 10^4 times greater in intensity than the incident field[29].

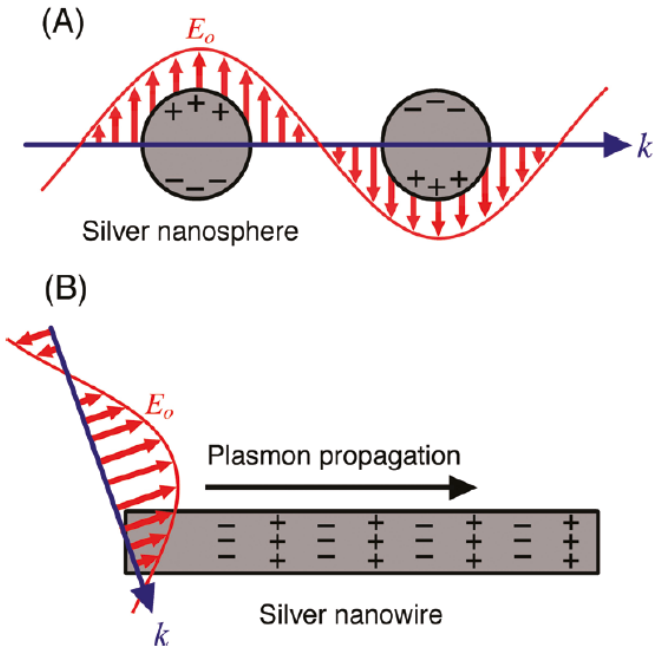

Figure 1. Schematic illustration of incoming light with amplitude E_0 and wavevector k stimulating (a) localized surface plasmon resonance, and (b) surface plasmon polaritons. Figure retrieved from reference [26].

Silver is perhaps the most important material in the field of plasmonics, offering many advantages over gold, aluminum, copper, and other metals[26]. It is known to support LSPR at visible and near-infrared (NIR) wavelengths with a high quality factor (Q)[26], has relatively simple chemistry allowing the synthesis of many different nanoparticle shapes[16], is

biocompatible[30], and has a relatively low cost. Therefore, the majority of research in plasmonics involves silver structures. Its main drawback is its susceptibility to oxidation when exposed to air[31]. A comparison of some of the commonly used metals for the fabrication of plasmonic nanostructures is given in table 1.

Metal	Plasmonic remarks	Chemical remarks	Nanostructure formation	Cost* (USD/lb.)
Aluminum (Al)	Good at UV wavelengths	Stable after surface passivation	Few nanostructures; mostly lithographic	0.75
Copper (Cu)	Interband transitions below 600nm	Easily oxidized	Few nanostructures	2.19
Gold (Au)	Interband transitions below 500nm; good Q factor; good at visible and NIR wavelengths	Stable	Many nanostructures	1333.25
Palladium (Pd)	Low Q factor	Stable	Many nanostructures	657.50
Platinum (Pt)	Low Q factor	Stable	Many nanostructures	1092.65
Silver (Ag)	Highest Q factor; good at visible and NIR wavelengths	Easily oxidized	Many nanostructures	19.89

*Table 1. Comparison of common metals used in plasmonic applications. *Price of commodity metals as of July 19, 2016. Table adapted from reference [26].*

2.1.1 Localized Surface Plasmon Resonance

Physically, the LSPR arises from a driven oscillation of conduction electrons across a nanostructure by an incident frequency of light, much like a driven harmonic oscillator. Within this analogy, the driving force is the oscillating electric field, the displacement of the spring is the displacement of the electron cloud from a static state, and damping forces arise from crystalline defects which add a resistance to the electron motion. A full physical description of the LSPR can be attained by using generalized Mie theory to solving Maxwell's equations. A full theoretical treatment can be found in reference [32] for both individual and aggregated metal spheres. Much of the physics for different shapes can be intuitively derived from the solution for

spheres. The main features of the LSPR can be found in the Mie theory result for extinction cross section σ_{ext} (absorption + scattering) for a spherical particle[32]:

$$\sigma_{ext} = \frac{24\pi^2 R^3 \varepsilon_m^{3/2}}{\lambda}\left[\frac{\varepsilon_i}{(\varepsilon_r + 2\varepsilon_m)^2 + \varepsilon_i^2}\right] \quad (1)$$

where R is the particle radius, λ is the incident wavelength, ε_m is the dielectric constant of the surrounding medium, and ε_r and ε_i represent the real and imaginary parts of the dielectric function of the particle material. Thus the interaction between light and a metal nanoparticle depends strongly on the dielectric function of the material, and the resonance condition occurs when the denominator in the bracketed term approaches zero. The extinction spectrum can be characterized experimentally using absorption spectroscopy.

The electric field on the surface of the particle is the origin of enhancement in LSPR based sensing applications. For a simplified treatment, we consider a spherical particle where the wavelength of light is much greater than the particle radius, i.e. R/λ « 1. This gives a quasi-static solution to Maxwell's equations, and the resultant electric field E just outside the particle is given by[27]

$$E(\vec{r}) = E_0\hat{\boldsymbol{z}} + \left(\frac{\varepsilon - \varepsilon_m}{\varepsilon + 2\varepsilon_m}\right)R^3 E_0\left(\frac{\hat{\boldsymbol{z}}}{|r|^3} - \frac{3z}{|r|^5}\vec{\boldsymbol{r}}\right) \quad (2)$$

Note that the dielectric function is wavelength dependent. Both equations (1) and (2) indicate that a resonance condition occurs when the real part of the dielectric function of the metal ε_r approaches $-2\varepsilon_m$. This is not possible for non-metals and insulator materials which typically have positive dielectric constants ranging from 1 to 50[33]. The real and imaginary dielectric functions of silver, gold, silicon, and silica are shown in figure 2 to illustrate the difference between metals, nonmetals, and insulators. Taking the surrounding medium to be air ($\varepsilon_m = 1$), resonance is met when $\varepsilon_r = -2$. Only silver and gold attain negative values of ε_r, and near resonance occurs for much of the visible range from 300nm to 500nm. LSPR coupling in nanoparticle dimers creates even more dramatic field enhancements within the hot-spot located in between the particles. Refer to figure 18 for a plot of the LSPR of a silver nanoparticle in a non-resonant

condition. When resonance conditions are met, the electric field can reach magnitudes as high as 100 times the incident field[29].

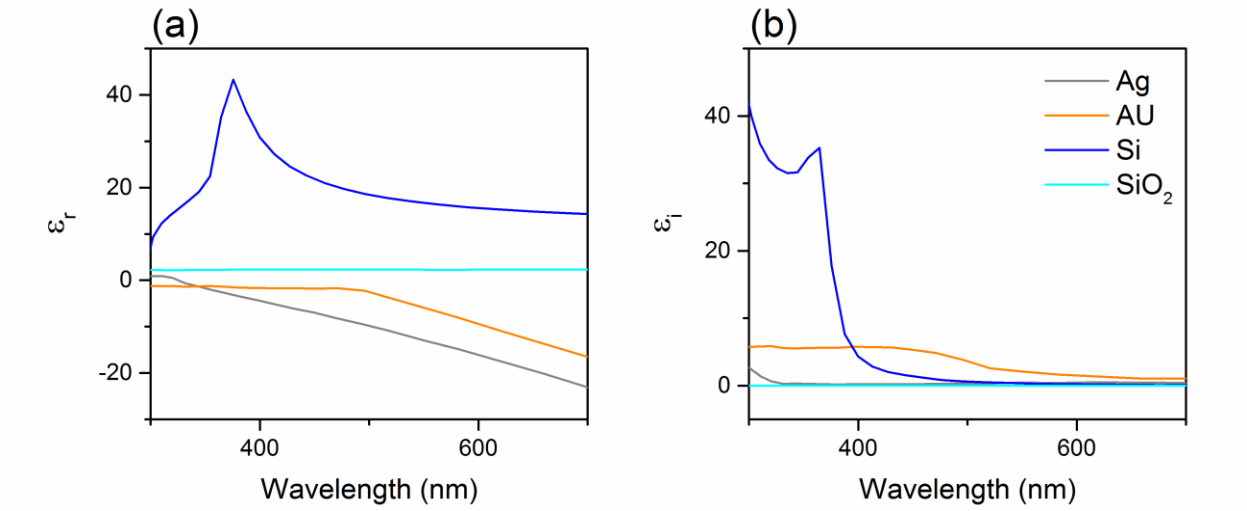

Figure 2. (a) Real and (b) imaginary parts of the dielectric function of Ag, Au, Si, and SiO_2 within the visible range. Data retrieved from references [34] for Ag and Au, [35] for Si, and [36] for SiO_2.

2.1.2 Applications

Plasmonics allows the guiding and manipulation of electromagnetic waves beyond the diffraction limit at the nanometer length scale[37]. The novelty of plasmonics as well as its specialized nature leaves many new technologies still standing to be realized, but it has rich potential in photonics and sensing. Some notable photonic applications include optical superlenses[38], invisibility cloak metamaterials[39], quantum optics[40], and including single photon transistors[41]. The integration of plasmonic materials may also lead to faster conventional electronics devices[42]. Plasmon-assisted light trapping is also one promising way to enhance the efficiency of thin film solar cells[9,43] and improve charge carrier generation[10].

The most developed and perhaps most useful application of plasmonics is in sensing. SPR spectroscopy can be used to monitor the kinetics of biological binding processes[27]. The local electric field enhancements due to the LSPR enable SERS, and metal enhanced fluorescence (MEF). In MEF, the fluorophore is both excited and emits photons, where the role of the surface plasmon is that of near-field modification of the fluorophores radiative decay

rate[13]. As a result the number of detected photons per fluorophore in DNA hybridization assays may be increased by a factor of 10 or more, and multi-photon processes have been reported to show 235-fold increase in emission intensity[44]. In SERS, the LSPR amplifies both the incident and Raman scattered light, providing immense Raman signal enhancement. This effect is explained in more detail in the following section.

2.3 Surface Enhanced Raman Spectroscopy

2.3.1 Raman Scattering

Raman scattering refers to an inelastic scattering process that can occur when a photon interacts with a molecule or atom. The majority of photons that scatter off matter are elastically scattered, in a process called Rayleigh scattering. A small fraction of the photons are scattered by an excitation, leading to a change in energy. Raman scattering involves scattering off vibrational energy states of a molecule, which are at infrared energies. Stokes and anti-Stokes Raman scattering result in either a redshift or blueshift in wavelength respectively, with the former being the more commonly occurring process. The energetics of these processes is illustrated in figure 3. Measurement of the frequency shift due to Raman scattering is a spectroscopic characterization method called Raman spectroscopy. This provides a molecular fingerprint and allows molecular identification by vibrational modes. Due to its dependence on molecular vibrational modes, this method is particularly suited towards large flexible organic and aromatic molecules.

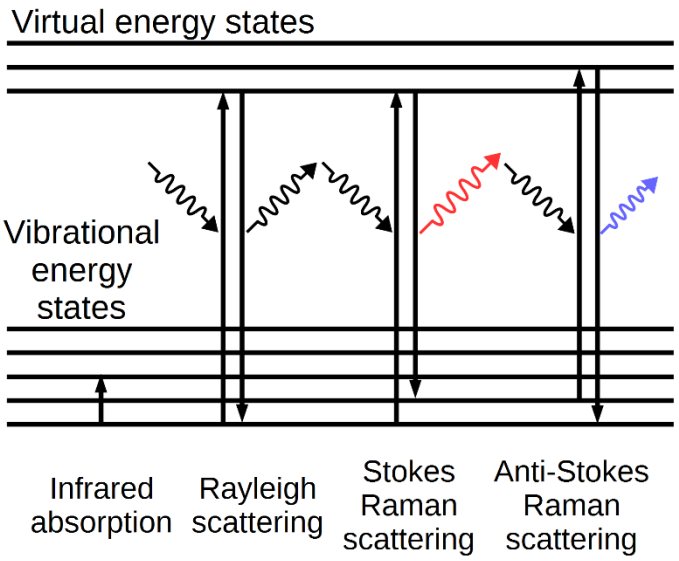

Figure 3. Energy level diagram of infrared absorption, and various possible photon scattering events off infrared excitation modes.

2.3.1 Surface Enhanced Raman Scattering

Surface enhanced Raman scattering is a phenomenon that occurs on roughened or nanostructured metal surfaces where the Raman signal of a molecule is greatly enhanced. The main cause of the signal enhancement is electromagnetic, arising from the action of the LSPR, but in some cases, a chemical enhancement is also involved[15]. The chemical enhancement arises from charge transfer interactions with chemisorbed species which are not plasmonic in nature but nonetheless provide a signal enhancement[15]. Therefore we focus our attention on the electromagnetic enhancement. In SERS, the large electric fields generated by the LSPR directly act on a target molecule within a so called "hot-spot", as if the molecule was excited by an amplified light field. Then, a second enhancement occurs to the Raman scattered photons by the same mechanism. Thus both the incident and Raman scattered fields are enhanced.

In Raman scattering, the scattered field intensity is linearly proportional to the incident field intensity. Let the incident field amplitude just outside the nanoparticle be represented by E, and the scattered field in the same position be E'. The distinction is required since the scattered field has a shifted wavelength [see equation (2)], and will thus experience the LSPR differently.

The final Raman signal intensity will be proportional to the product of E^2 and E'^2. For small Raman shifts, we can use the approximation $E \approx E'$. Thus, the final signal intensity is proportional to $|E|^4$, and the enhancement factor (EF) is proportional to $|E/E_0|^4$. This is the etymology of the widely quoted E^4 enhancement in SERS.

2.3.2 SERS Enhancement Factors

The magnitude of the SERS signal is ultimately why the development of SERS substrates exists. In order to compare substrates with one another, it is necessary to introduce an experimentally practical definition of the enhancement factor. The EF is historically a contested quantity, as it is often estimated incorrectly with disparities between authors being as high as several orders of magnitude[45], yet it is arguably the most important quantity in characterizing a SERS substrate. We refer the reader to a broad analysis published by Le Ru et al.[46] which clarifies several of the issues regarding the determination of EFs, and provides a rigorous derivation to understand their origins. The EF fundamentally arises from the single-molecule enhancement factor (SMEF), which is the SERS enhancement of a molecule at a point. The SMEF depends on the local geometry of the SERS substrate, as well as its orientation relative to the laser polarization and direction.

The SMEF is clearly more suited to theoretical estimations of the EF, as it depends on many parameters not viable to be obtained experimentally. Thus the most commonly used definition of the EF is

$$\mathrm{EF} = \frac{\mathrm{I_{SERS}}/\mathrm{N_{SERS}}}{\mathrm{I_{RS}}/\mathrm{N_{vol}}} \tag{3}$$

where I_{SERS} and I_{RS} are the intensities of identical bands for the SERS and normal Raman scattering spectra, N_{vol} is the number of molecules probed in the normal Raman measurement, and N_{SERS} is the number probed in the SERS measurement. This EF can be shown to be derived from the SMEF by spatial and orientation averaging of the SMEF on the SERS substrate[46]. While this definition is better suited to characterizing substrate performance, it remains difficult to properly characterize both the scattering volume and N_{SERS}. N_{SERS} comprises of both molecules adsorbed on the metal surface and those floating in the surrounding medium, however

the latter is often ignored since the long range enhancement of SERS is negligible compared to surface sites. While estimates of adsorbed molecule surface density are possible for self-assembled monolayers[24] or by use of electrochemical measurements[47], estimation of N_{SERS} still remains the largest source of uncertainty in determining EFs[46]. When taking N_{SERS} to be strictly molecules adsorbed on the metal surface, N_{SERS} and N_{vol} can be defined as follows

$$N_{SERS} = N_s \mu_s A_M A_{eff} \tag{4}$$

$$N_{vol} = C_{RS} H_{eff} A_{eff} \tag{5}$$

where N_s is the surface density of nanostructures producing the enhancement with respect to the SERS substrate, μ_s is the surface density of molecules adsorbed on the nanostructure surfaces, A_M is the surface area of an individual nanostructure, A_{eff} is the area of the effective scattering volume with respect to the substrate, C_{RS} is the concentration of analyte, and H_{eff} is the height of the effective scattering volume. Equation (3) then becomes

$$\mathrm{EF} = \frac{\mathrm{I_{SERS}} \mathrm{C} \mathrm{H_{eff}}}{\mathrm{I_{RS}} \mathrm{N_s} \mu_\mathrm{s} \mathrm{A_M}} \tag{6}$$

Note that A_{eff} cancels and the only parameter which captures the geometry of the scattering volume is H_{eff}.

Both the SMEF and the EF emphasize intrinsic substrate characteristics, and as a result depend on quantities which are difficult to characterize experimentally. Naturally, the measurement of SERS signals will involve an analyte at concentration C_{SERS} producing a Raman signal of intensity I_{SERS}. Prior to any intrinsic substrate considerations, consider measuring the Raman signal of intensity I_{RS} of an analyte at concentration C_{RS} in the absence of a SERS substrate. The analytical enhancement factor (AEF) is then defined as

$$\mathrm{AEF} = \frac{\mathrm{I_{SERS}}/\mathrm{C_{SERS}}}{\mathrm{I_{RS}}/\mathrm{C_{RS}}} \tag{7}$$

This definition is useful in practical application, however it ignores several factors. In particular, it depends on the adsorption properties of the analyte and surface coverage of the SERS probe. While the AEF is not a good characterization of the SERS substrate, it represents a simple and reproducible measurement which is particularly suited to the measurement of SERS active liquids[46].

2.3.3 Applications of SERS

The high sensitivity of SERS coupled with the development of surface preparation techniques has led to SERS being employed in a wide range of analytical systems. Some of the conventional detection applications for SERS include in-vitro and in-vivo glucose sensing[48], anthrax biomarker detection[49], overdose drug testing in saliva[50], and explosive detection[51]. SERS may also be integrated into other systems to perform real-time catalytic reaction monitoring[52], or environmental monitoring when decorated on fibre optic coatings[53]. SERS substrates also serve as a general non-specific detection platform for compatible molecules, and enable trace detection.

2.4 SERS Substrates

In the past, SERS was performed directly on colloidal solutions[14,15]. These days, the development of SERS active substrates drives research, with the eventual goal of commercialization. The variety of SERS substrates is reported to date is enormous, but the fabrication of substrates can be classified into two categories; bottom-up methods, which use self-organization and aggregation processes, and top-down methods, which generally consists of miniaturization of larger structures[17].

2.4.1 Bottom-Up Fabrication

The bottom-up approach to substrate fabrication is the most popular as it is simpler, usually does not involve specialized equipment, and has a low cost. However, its main drawback is that it relies on difficult to control and atmospherically sensitive dynamical processes which result in lower short range substrate uniformity, and therefore lowered signal reproducibility[54].

Nanoparticles are typically synthesized through wet chemistry, and then immobilized onto a solid support via self-assembly, or direct transfer[54]. This allows one to freely choose the type of nanoparticle deposited. Chemical synthesis methods can produce a diverse variety of possible shapes[16,55], which allows one to choose the LSPR profile desired. Chemical-free nanoparticles are also available via laser ablation synthesis techniques, although with greater polydispersity[17]. An alternative to deposition is to grow nanostructures on a solid support. This is achieved via electroplating a roughened substrate[56], or growing nanoparticles directly on a surface by using, for example, a mixture of silver nitrate and hydrofluoric acid[57].

Self-assembly processes may be used to chemically or electrostatically immobilize nanoparticles on a substrate. First, the surface of the support is functionalized with a chemical functional groups using a surface polymerization procedure, then the functionalized surface is immersed in a nanoparticle suspension. The properties of the immobilization surface, the properties of the nanoparticles, and the interaction of the nanoparticles with the surface determine final nanoparticle film outcome. Some experimental factors include the chemical functional groups chosen, the immobilization time, the surface adsorbates on the nanoparticles, and the solution conditions including concentrations, ionic strength, pH, and temperature[17]. Self-assembly results in monolayer or multilayer nanoparticle films. In many cases, the nanoparticles form clusters on the substrate, which lead to a large presence of dimer hot-spots. As a result, enhancement factors of up to 10^{10} are possible, allowing for single molecule detection[46]. The two major types of self-assembly immobilization are covalent and electrostatic.

Covalent immobilization is performed by functionalizing a surface with either amine or thiol groups to covalently bond nanoparticles to the surface[58]. This method allows the immobilization of both charged and uncharged particles without the need for particle functionalization. This is particularly suited for silver due to its high affinity towards thiol and amines. For silica substrates, it is common to perform silanization of the surface using thiol or amine terminated alkoxy silanes such as (3-aminopropyl)triethoxysilane (APTES), (3-mercaptopropyl)trimethoxysilane (MPTES), or (3-aminopropyl)dimethylmethoxysilane (APDMS)[59]. Compared to other aminosilanes, APTES provides the greatest density of surface charge, with almost twice the measured surface potential than its closest molecular analog (3-

aminopropyl)trimethoxysilane (APTMS)[59]. The same study showed that despite this, the density of immobilized nanoparticles was almost the same, with APTES being only slightly higher[59]. If silanization is not possible on the substrate, polyelectrolytes like poly(allylamine hydrochloride) (PAH)[60], or poly(ethylene imine) (PEI)[61] can be polymerized on a surface to provide the functional groups.

Electrostatic immobilization uses either the natural charge of particles in solution, or particles stabilized by a charged capping agent, and immobilizes them onto an oppositely charged substrate. Similar to covalent immobilization, substrates are functionalized with molecules which provide a surface charge. The distinction here is that the nanoparticles do not covalently bond. Some functionalization molecules include poly(vinylpyridine)[62], poly(vinylpyrrolidone) (PVP)[63], and polymer dendrimers[18]. Nanoparticles may either be synthesized in the presence of the desired capping agent, or a surface displacement reaction may be introduced. Some common capping agents used for silver include PVP[55,64], citrate[65,66], and hexadecyltrimethylammonium bromide (HTAB)[30].

Directly dropping nanoparticles onto a substrate and allowing them to dry results in a rudimentary SERS substrate, albeit with a poorly defined surface. However, this method was reported to produce highly regular nanostructures when done on a wrinkled polydimethylsiloxane (PDMS) support, in a so called "wrinkle-confined drying" process[67]. Nanoparticles can be transferred onto a solid substrate from a liquid-liquid or liquid-air interface using the Langmuir-Blodgett technique. In Langmuir-Blodgett deposition, nanoparticles are dispersed in chloroform, and then sprayed onto a water bath to form a monolayer at the water-air interface. A barrier then compresses the monolayer with controlled force, and the substrate is drawn upwards through the monolayer. With care, this method can result in very well defined monolayers[68], and multiple depositions can be performed to make combinations of nanoparticle and supporting molecule layers[18]. Microcontact printing also enables direct transfer of nanoparticles to a substrate. First, nanoparticles are assembled in a monolayer at a liquid-air interface, then they are transferred to a PDMS stamp pad and pressed onto a substrate[69]. The nanoparticle monolayer inherits the patterns found on the PDMS stamp, and regular array structures are possible.

2.4.2 Top-Down Fabrication

Top down techniques make use of lithography, etching, and templates to produce LSPR hosting nanostructures. The most commonly employed lithographic method is electron beam lithography (EBL). EBL is able to make structures much smaller than possible with photolithography, due to the short de-Broglie wavelength of electrons. Both positive and negative resists may be used. The electron beam selectively etches off regions of the resist to create nanostructures, and then vapor deposition is used to metallize the surface[54] in one of two follow-up procedures depicted in figure 4a. EBL has used to produce nanohole array[70], which have promising applications in the integration of SERS and microfluidics[71]. Combining lithography and self-assembly has allowed the formation of period nanoparticle arrays, depicted in figure 4b. By changing the size of the lithographically etched holes, Yan et al. were able to control the number of nanoparticles which assemble in each hole[72].

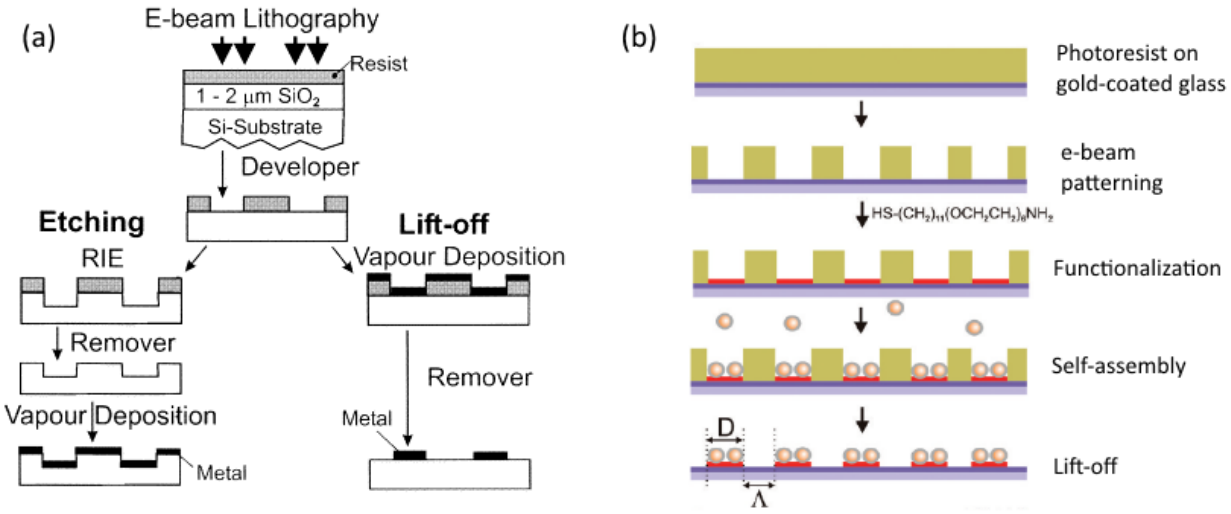

Figure 4. Electron beam lithography fabrication of SERS substrates. (a) Two avenues of post lithography treatment in order to metallize the surface for SERS, adapted from reference [73]. (b) Combination of EBL and self-assembly to produce arrays of nanoparticle clusters, adapted from reference [72].

While lithography is able to produce highly regular and reproducible nanostructures, mass production is not feasible. Template directed synthesis is a promising approach to overcome this challenge. Template deposition mainly comes in two flavors: electrochemical and vapor deposition. In electrochemical deposition, anodic aluminum oxide (AAO) form

hexagonally arranged nanoholes in a processes known as anodization. These nanoholes are then used as a template for metal deposition before being chemically etched away, leaving an array of standing nanopillars[74]. Vapor deposition can directly form a SERS substrate as a bottom-up approach. When a thin film of silver is deposited on a flat surface, the evaporated metal tends to cluster, forming a nanoparticle monolayer[54]. In the top-down case, vapor deposition is performed in the presence of a mask, which causes preferential growth of the nanostructures in places not covered by the mask. The mask is then removed leaving behind a nanostructured surface. In the most common type of substrate employing vapor deposition, a self-assembled hexagonally close packed array of silica nanospheres act as a mask, and nanotriangles are formed beneath the mask in a process named nanosphere lithography[75].

2.4.3 Comparison of SERS Substrates

The requirements of a good SERS substrate include high sensitivity, spot-to-spot and substrate-to-substrate signal reproducibility, and long term stability[76]. Silver readily oxidizes in air[31], while gold is stable. However, silver has been shown to have greater SERS enhancements over gold[19]. The cost and scalability in fabrication must also be considered for the mass adoption of SERS. Mass production is easy with colloidal self-assembly as multiple substrates can be made in parallel with a single suspension of nanoparticles. However, the structures formed are irregular at nanometer length scales, and signal reproducibility is sacrificed. Additionally, eventually the nanoparticles become depleted and a new suspension must be used, with no guarantee that they will be exactly the same. Top-down methods resolve the signal reproducibility issues, and are therefore good in quantitative detection applications. However, fabrication is time consuming and costly. An overview and evaluation of several selected SERS substrates is presented in table 2. Evidently, the EF solely depend on the structure of the substrate, and irregularity does not play a role in the substrate sensitivity.

Substrate	Fabrication Method	Cost	Scalability	EF	Reference
Ag NP Monolayer	Self-assembly, electrostatic	Low	Very good	10^8	[77]
Au NP Monolayer	Self-assembly, covalent	Low	Very good	10^6	[78]
Ag nanocube monolayer	Langmuir-Blodgett	Medium	Good	10^7	[68]
Ag nanowire monolayer	Langmuir-Blodgett	Medium	Good	10^9	[79]
Ag NP dimer	EBL, angle evaporation	High	Poor	10^9	[80]
Ag NP cluster array	EBL, self-assembly	High	Poor	10^6	[72]
Au nanohole array	EBL	High	Poor	10^5	[70]
Au nanodisk array	EBL	High	Poor	10^3	[70]
Vertical Ag nanowire array	AAO template	Medium	Good	10^6	[81]
Ag nanotriangle array	Nanosphere lithography	High	Good	10^8	[75]

Table 2. Comparison of selected SERS substrates. Some of the references listed have reported lower EFs for different fabrication parameters, such as array spacing, number of depositions, etc. EFs shown here are the largest values attained in the corresponding report.

2.5 Conclusions and Outlook

SERS substrates are an exciting technology to emerge from plasmonics, which enable molecular sensing at extremely low concentrations. Self-assembled monolayers are a low-cost, highly scalable approach to SERS substrates recently reported to be capable of single molecule detection[20]. Silver nanoparticle monolayers are a versatile substrate, with a wide variety of synthesis and immobilization schemes. Despite their prevalence in research, most authors focus on the goal of the SERS substrate itself, and therefore neglect to report important experimental parameters which affect deposition kinetics. The dynamical processes that occur during nanoparticle immobilization is of interest as they determine the final structure of the monolayer. Much of the science has been established in the context of diffusive transport[60], and experimental data is slowly building up to validate these models[17]. The development of SERS substrates and the study of their properties is an exciting field of research which has potential to benefit a wide range of practical applications.

Chapter 3: Silver Nanoparticle Monolayers for Surface Enhanced Raman Spectroscopy

3.1 Summary

Silver nanoparticles are synthesized by a seeded ascorbic acid reduction of amine complexed silver. Nanoparticle monolayers are fabricated by colloidal self-assembly onto a polyelectrolyte functionalized glass slide. UV/vis absorption spectroscopy is used to characterize the optical properties of both the colloid and monolayers, and SEM imaging is used to inspect the morphology of the monolayers. Using these techniques, the time dependent properties of monolayer formation is reported. The monolayers are then used as SERS substrates for the trace detection of a target dye molecule rhodamine 6G a 632.8nm laser excitation. The detection limit for R6G was found to be 10^{-10}M, or 0.4ppb, and single molecule sensitivity is likely achieved.

3.2 Introduction

Metal nanoparticles serve as the sensing platform in SERS spectroscopy, metal enhanced fluorescence[13,82], and in immunosensing of biological markers[11,12]. The transition metals silver and gold are the most widely used due to both cost and favorable plasmonic behavior, but a few other metals like platinum and palladium have been explored[83]. Silver exhibits improved SERS enhancement factors over gold[19], but is more difficult to achieve monodisperse particle sizes during synthesis. Additionally, silver is more reactive than gold, and its rapid oxidation is preventing the commercialization of silver based SERS substrates[31]. Gold based substrates, however, are commercially available, due to their greater long term storage capabilities.

The formation of metal nanoparticle monolayers via colloidal self-assembly for SERS was first described in 1995 by Griffith et al.[84], and has since been replicated by many authors with a variety of different polyelectrolytes, nanoparticles, and solution conditions. Self-assembly is low cost and scalable approach to the fabrication of SERS substrates, compared to other approaches involving lithography[75] or etching[85], and results in monolayers of nanoparticle clusters which contain structures on a scale not achievable by these other methods. In fact,

enhancement factors can reach the order 10^{10} for a silver nanoparticle dimer[86], while reported EFs are on the order of 10^7 for a silver nanotriangle array produced by lithography [25]. In some cases, self-assembled substrates have been reported to show single-molecule sensitivity[20,87].

In this chapter, silver nanoparticles are synthesized, and monolayers are formed via colloidal self-assembly onto a (3-aminopropyl)triethoxysilane (APTES) functionalized glass slide. The synthesis uses ascorbic acid to reduce amine complexed silver onto silver seed surface. This method, developed in our lab, causes relatively slow growth of the seed particles and results in a well monodispersed colloid. The optical and structural properties of the monolayer are characterized, and the kinetic aspects of monolayer formation are studied, as an understanding of them leads to surfaces with well controlled surface density and structure. The substrates are then used for SERS detection of the dye molecule rhodamine 6G (R6G) in solution phase. The enhancement factor of the substrate is estimated, and single molecule sensitivity is demonstrated using successive dilutions of R6G.

3.3 Materials and methods

3.3.1 Materials

Silver nitrate Premion^{TM} grade >99.9995% ($AgNO_3$), trisodium citrate >99% (TSC), ascorbic acid >99% (AA), and sodium borohydride>99.99% ($NaBH_4$) were obtained from Alfa Aesar. Polyvinylpyrrolidone Mw = 55K (PVP), (3-aminopropyl)triethoxysilane>99% (APTES), and rhodamine 6G >99% (R6G) were obtained from Sigma-Aldrich. Ammonium hydroxide ACS grade, hydrogen peroxide 30% in water, sulfuric acid ACS grade, and glass slides were obtained from Fisher Scientific. Ultra-pure water obtained from a Durpro filtration system ($\rho > 18.2M\Omega$) was used throughout the experiments.

3.3.2 Synthesis of Silver Nanoparticle Seeds

Seeds were synthesized by preparing a 100mL solution of 0.3mM TSC and 0.25mM AgNO3 in an ice bath. The solution was left to cool with stirring for over 10min, then 3mL 10mM $NaBH_4$ was added drop wise every 5s. The solution was stirred for an additional 30min in the ice bath then stored in a household refrigerator at 4°C for up to 1 month prior to use. The resultant solution

consisted of 4nm diameter seeds. Seed concentration was estimated to be $1.1x10^{-7}$M, based on the estimated concentration of NPs after the full synthesis.

3.3.3 Synthesis of Silver Nanoparticles

Monodisperse silver nanoparticles were synthesized by a seeded ascorbic acid reduction of silver-amine complex. PVP and TSC are surfactant molecules which act as stabilizers for the nanoparticles during growth. Silver-amine complex ($Ag[NH_3]^{2+}$) was prepared by adding ammonium drop wise into a 0.12M solution of $AgNO_3$ until the solution became clear. Nanoparticles were synthesized by adding 2mL 20mM PVP, 12mL 30mM TSC, 2mL 0.12M $Ag(NH_3)^{2+}$, and 0.4mL silver seed into 200mL water with stirring. Then, 3mL 0.1M ascorbic acid was added drop wise roughly every 10s. The solution changed from transparent citrine, to auburn, to opaque copper, while slowly developing a gray cloudiness.

3.3.4 Fabrication of Silver Nanoparticle Monolayers

Glass slides were cleaned in boiling Piranha etch ($1H_2O_2$:$4H_2SO_4$ vol.) diluted to 10% in water at 90^{o}C for 1h. A solution of 1% vol. APTES was prepared during this time and allowed to hydrolyze for >15min. The slides were removed from the Piranha, rinsed with water, and immersed in the APTES solution upright for 1h. The silane end of the APTES molecule integrates into the surface matrix of the glass slide in a process known as silanization. This method has been shown to be effective at producing a single monolayer of APTES onto the glass surface with minimal defects[59,88]. The substrates were then rinsed with water, and dried in a convection oven at 80^{o}C for 2h. Ag NP monolayers were formed by NP immobilization on the functionalized slides by immersion in Ag NP solution upright for at least 48h or otherwise specified. The substrates were then removed, rinsed with water, and then drawn out of water bath by a dip coater at 1mm/min lifting speed to ensure even drying. The substrates were used immediately after drying for the study to minimize oxidative effects from atmospheric exposure[31]. A schematic of this process is shown in figure 5.

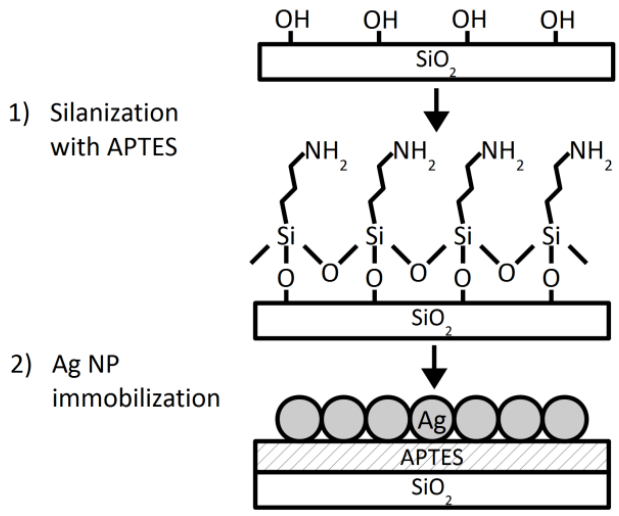

Figure 5. Self-assembly process for the immobilization of silver nanoparticles in a monolayers. The negatively charged particles are attracted to the positively charged amine tails of the APTES polyelectrolyte.

3.3.5 Instrumentation and Characterization Methods

UV/Vis absorption spectra were acquired by a Shimadzu UV-2501PC, using a slit width of 1nm. A bare glass slide was used as the reference for substrates, and a water filled cuvette was used for solutions. Scanning electron microscopy was performed on a ZEISS LEO 1550 FE-SEM. SEM image analysis was performed using the Gwyddion 2.44 software package. Raman spectra were acquired on a Renishaw Raman Dual System 1000. The Raman excitation source was a helium-neon laser at a wavelength of 632.8nm focused using a 50x objective lens. SERS measurements were taken by dropping 3μL of analyte onto the substrate, and smearing the droplet using a glass cover slip of approximately 4mm x 4mm to even the distribution of analyte on the substrate, and prevent refractive light loss. This configuration is depicted in figure 11b. All Raman measurements used the same neutral density filter to achieve a laser power of 4.53mW. Spectral analysis and peak processing was done using the OriginPro 2015 software package.

3.3.6 Determination of SERS EF

A glass cover slip was used to smear a droplet of analyte on the SERS substrate, so the height of the scattering volume approximately depends on the diameter of nanoparticles, since the cover

slip is supported by the rigid nanoparticles. To keep the height of the scattering volume consistent between measurement of I_{SERS} and I_{RS}, a fine line of nanoparticles was wiped away on a SERS substrate using a wet laboratory tissue, and I_{RS} was measured within the scratch. The cover slip was supported on either side of the line by the nanoparticle monolayer. This avoids a strict characterization of H_{eff}, which is instead approximated by the nanoparticle diameter.

Since it was experimentally unfeasible to determine the adsorbed density of R6G on the silver surface, EF was not calculated according to equation (6). Instead we start with equation (3) and introduce an alternative definition of N_{SERS}, called N'_{SERS}

$$N'_{SERS} = \left(H_{eff}A_{eff} - N_s A_{eff}\frac{1}{6}\pi d_p^3\right) C_{SERS} \tag{8}$$

The term in brackets is simply the scattering volume minus the volume occupied by nanoparticles in the scattering volume. N'_{SERS} is simply the number of molecules in the gaps between nanoparticles, assuming a uniform distribution of the analyte molecule equivalent to its solution concentration. While this definition ignores the surface adsorption of analyte, it is entirely in terms of experimentally acquired values. Substituting N_{SERS} for N'_{SERS}, equation (3) becomes

$$EF' = \frac{I_{SERS}/C_{SERS}}{I_{RS}/C_{RS}}\alpha \tag{9}$$

which resembles the AEF with a factor α which accounts for the space occupied by the nanoparticles. Assuming a uniform height monolayer, we take $H_{eff} = d_p$, in which case α is

$$\alpha = \frac{1}{1 - N_s\pi d_p^2/6} \tag{10}$$

3.4 Results

3.4.1 Bulk Solution Characteristics

The bulk nanoparticle solution appears as a semi-transparent mixture of smoky gray and copper that is attributed to the plasmon resonance of the nanoparticles[17]. UV/vis absorption spectroscopy reveals the quantitative nature of the solutions LSPR profile, shown in figure 6 for various solution dilutions. This method can be used to estimate particle size with peak position and monodispersity with peak width[89]. The profile shows a single symmetrical peak, centered at 413nm, which indicates spherical particles[16]. The concentration of the solution was estimated by taking the average particle diameter, determined using SEM in figure 7, to calculate the amount of silver per particle, and dividing the total amount of silver added to the solution by the amount of silver per nanoparticle. The bulk concentration of the original solution was found to be $1.0 \times 10^{14} L^{-1}$. An experimental linear dependence of the peak absorbance on particle concentration was found, shown in figure 6b, in agreement with a theoretical treatment[89]. It is therefore possible to estimate the solution concentration using the UV/vis absorption peak height, given the same peak position and spherical particles.

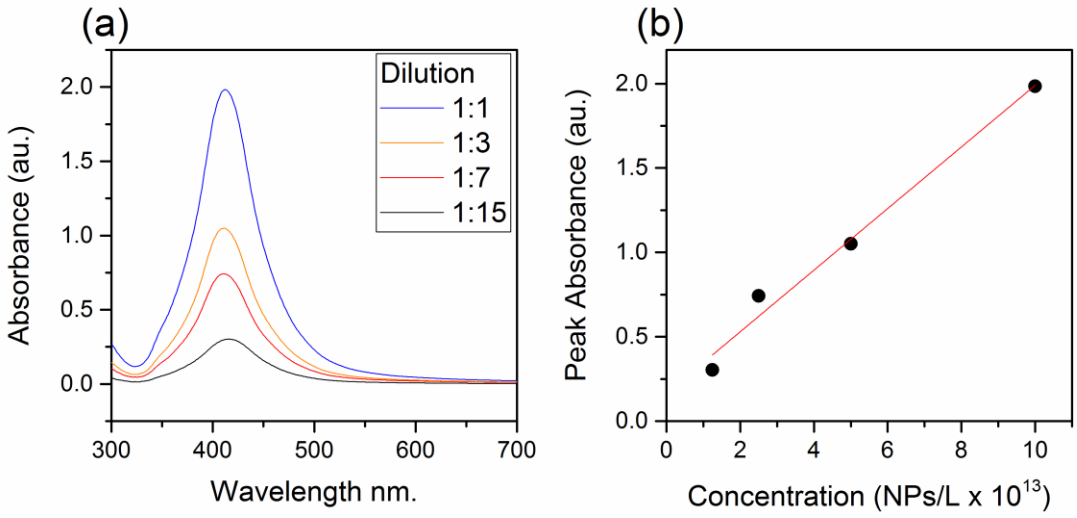

Figure 6. (a) The absorption spectrum of the silver nanoparticle solution dilutes at various ratios in water. The peak absorbance occurs at 413nm. (b) The relationship between the peak absorbance and the nanoparticle concentration. The red line shows a linear fit with $R^2 = 0.98$.

3.4.2 Substrate Characteristics

Nanoparticle monolayers appear as an olivine transparent coating with defects located at the edge of the uncoated region. The defect region was located at the water-air interface of the solution during immobilization, and is most likely a result of a slight decrease in solution volume from evaporation over the 48h immobilization period. The substrates are otherwise entirely uniform to the eye. SEM imaging was used to study the structure of the nanoparticle substrates, shown in figure 7. Particles are found to be quasi-spherical, immobilized on the substrate in clusters with no vertical particle stacking. A histogram of particle sizes reveals a Gaussian distribution centered at 45.1nm diameter in with a standard deviation of 7nm, in agreement with the UV/vis absorption peak position. This clustered structure is advantageous for SERS applications, as the greatest electromagnetic fields are found in hot-spots within the nanoscale gaps in between particles [90].

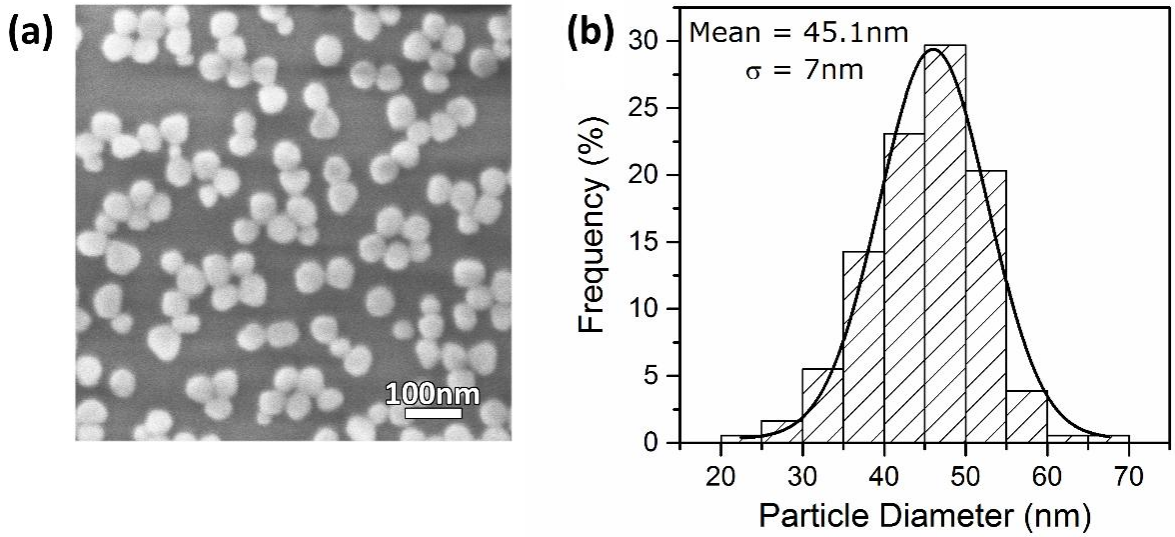

Figure 7. (a) SEM micrograph of a SERS substrate following 48h of immobilization. (b) Particle size histogram with a Gaussian curve fit. Diameters were determined by measuring the distances across particles using Gwyddion. Since particles are found to be quasi-spherical, this method yields an approximate diameter per individual particle, and a statistical treatment is used.

Spot-to-spot signal reproducibility is an outstanding issue in the development of SERS substrates, and it is necessary to have a uniform density of hot-spots across the substrate so that there is a consistent number of them under the laser excitation during a SERS measurement. To

evaluate substrate uniformity, the nanoparticle and hot-spot densities were determined by manual counting using SEM images on 3 different substrates at 4 positions per substrate, using images spanning 2.16μm^2 corresponding to around 360 particles. Hot-spots were counted wherever a particle came into contact with another particle, with no visible gap in between. The distribution of these quantities is plotted in figure 8. Generally, greater particle coverage corresponds to a greater presence of hot-spots as expected. Average nanoparticle density was 171/μm^2 with a standard deviation of 5μm^{-2}, and average hot-spot density was 151/μm^2 with a standard deviation of 5μm^{-2}. Thus over areas of at least 2μm^2, the substrate shows good spot to spot structural uniformity. As a result, the SERS signals are consistent at higher concentrations, and peak height varied less than 10% as can be seen in figure 12b.

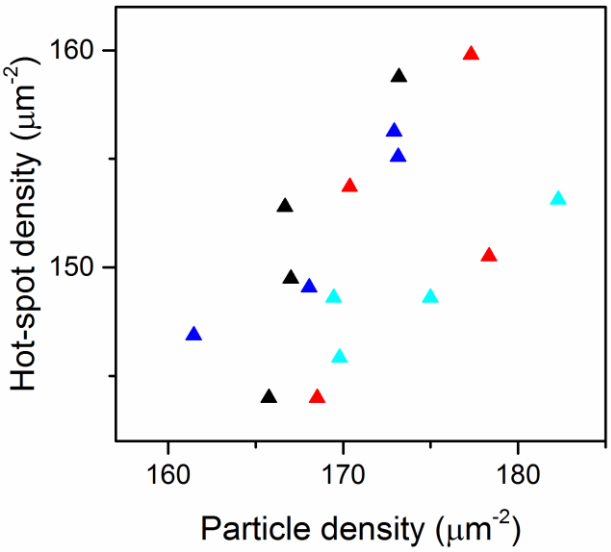

Figure 8. Distribution of the hot-spot density and particle density. Color groups represent individual substrates, and points of the same color were measured at different positions on a substrate.

Following the result of section 3.4.1, the magnitude of the absorbance of the substrates may be used as an indicator of nanoparticle surface density on the substrate. Figure 9 shows the absorbance spectra of substrates after various immobilization times. The substrates have a primary double peak feature at around 375nm, and a second bump above 650nm. The blueshift of the primary peak from the solution spectrum is due to the change in refractive index from water to air, which blueshifts the light apparent to the nanoparticles in solution[18]. The blue side

of the double peak corresponds to the regular plasmon resonance, and the red side arises from plasmon modes depolarized from the original excitation[33]. As the immobilization time increases, the blue side of the double peak becomes more prevalent, as well as the absorption feature at 650nm. Both of these effects arise due to the coupling of plasmon resonances between neighboring particles as nanoparticle density increases. This coupling both inhibits the depolarization of plasmon excitations, and produces a higher order oscillation mode which manifests as an absorbance peak in the red wavelengths[18,91].

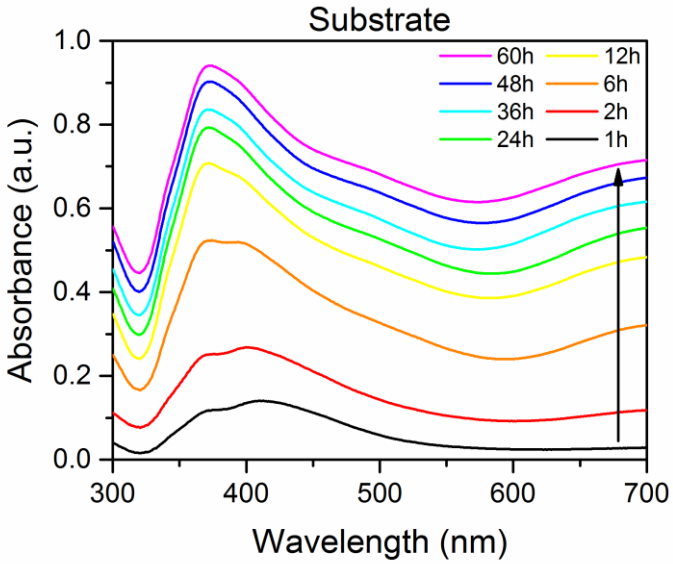

Figure 9. UV/vis absorption spectra of nanoparticle monolayer substrates after various immobilization times. Acquisition slit width was 1nm. All spectra are offset by an absorbance of 0.05 to show their distinct shape, however the spectra for 60h, 48h, and 36h overlap almost entirely. The arrow indicates direction of increasing time[17]

3.4.3 Kinetics of Nanoparticle Immobilization

The formation of silver nanoparticle monolayers by adsorption onto cationic polyelectrolyte surfaces has been systematically studied by Oćwieja et al.[17,92] on poly(allylamine hydrochloride) modified mica, where the general properties are applicable to most combinations of polyelectrolyte, surface material, and nanoparticle solution conditions. In the case of solution based self-assembly, the nanoparticles are negatively charged which attracts them to cationic electrolyte, and particle adsorption is based on diffusion transport processes[92]. At short immobilization times, particle coverage is proportional to $t^{1/2}$, while at longer times, interparticle

repulsion results in saturation of the surface, and prevents the buildup of additional particle layers[93]. Coverage is measured by the dimensionless quantity Θ, determined by the equation

$$\theta = \pi d_p^2 N_s/4 \tag{11}$$

where d_p is the particle diameter, and N_s is the average number of particles per unit area (surface density), measured in units μm^{-2}. Coverage is distinct from surface density, and provides a measure of the available nanoparticle surface area. The early kinetics of particle adsorption at the surface can be described by the equation[92]

$$N_s = 2\left(\frac{D}{\pi}\right)^{1/2} t^{1/2} n_b \tag{12}$$

where D is the diffusion coefficient ($\mu m^2/s$), t is the time (s), and $n_b(\mu m^{-2})$ is the bulk number concentration of particles. Equation (12) is based on a diffusion based transport model of particle adsorption, and does not completely capture the dynamical processes of particle adsorption in the case of nanoparticles, where the electric double layer and surfactants play a role during particle-particle collision.

Figure 10a shows the dependence of the nanoparticle density and absorbance on immobilization time. Initial particle uptake rate has been shown to be related to solution parameters including nanoparticle concentration and ionic strength as these affect the diffusion of particles in solution, while final coverage depends only on the nanoparticle size and interaction range[17]. This finding is in agreement with what is observed in the SEM images in figure 10(c-e), which reveal the nature of particle uptake. Initially, individual particles are found on the substrate during the diffusive time period, with interparticle repulsion preventing the buildup of agglomerates. Saturation of the substrate is achieved mostly by "sticky" particle-particle collisions, which causes the formation of clusters, and indicates that there is an attraction for very short interparticle spacing. This is the reason why the $t^{1/2}$ dependence of particle loses validity before the saturation point. Based on the plots in figure 10a, saturation is reached after 24h, at the final average density of $171 \mu m^{-2}$ as observed in figure 8. The final density varied by

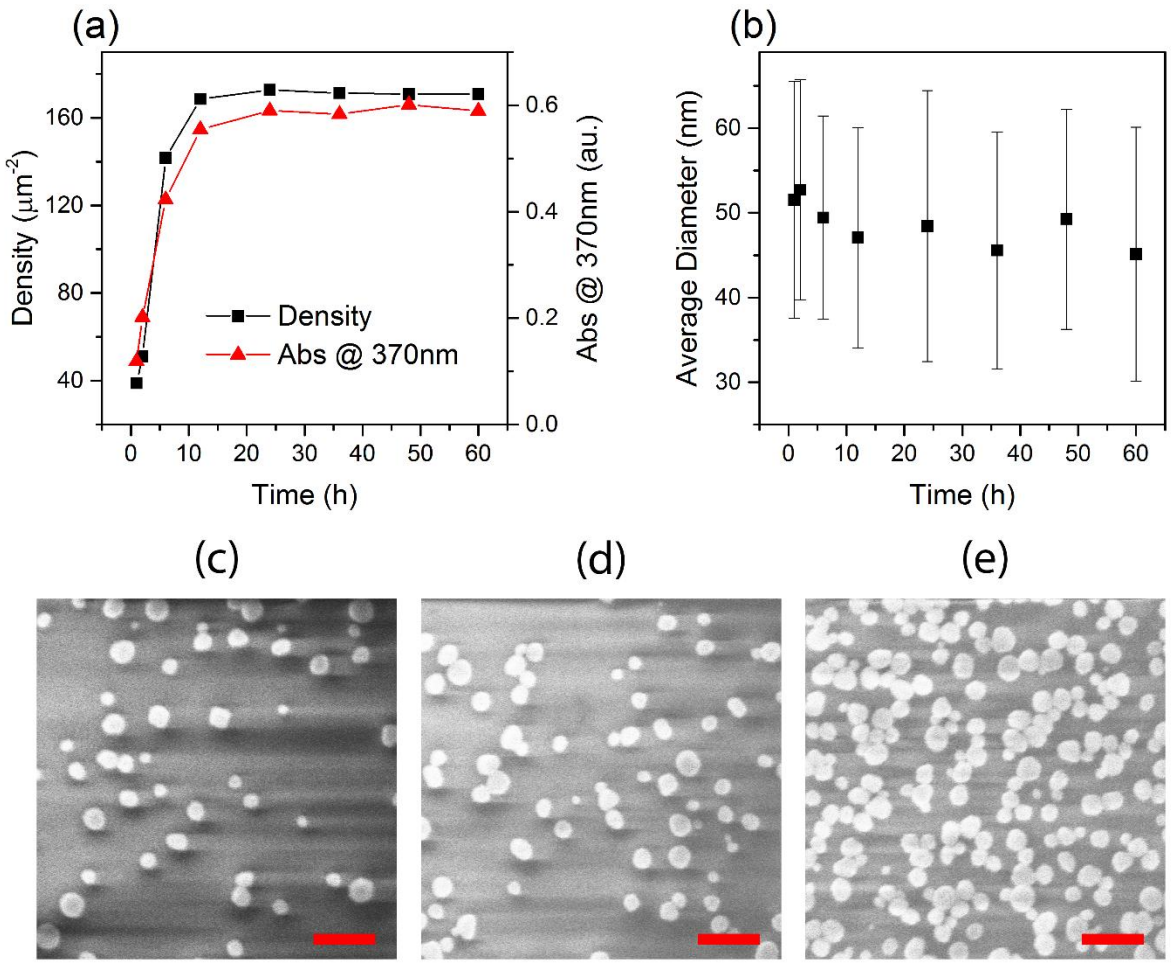

Figure 10. Effect of coating time on (a) substrate nanoparticle density and absorbance at 370nm, and (b) average nanoparticle diameter. SEM images of substrate after (a) 1h, (b) 2h, and (c) 6h. Scale bars represent 200nm.

less than 3% between all the saturated substrates, and the final coverage θ was calculated to be 0.297, in agreement with the typical reported values for particles of this size[17]. Interestingly, the average particle diameter was noted to decrease over time until saturation, plotted in figure 10b. This is explained by the fact that smaller particles are more likely to be captured when the surface density is higher, which makes candidate capture sites smaller. Therefore a standard time of 48h was chosen as the standard for SERS substrate fabrication, in order to exclude any lingering short term effects.

3.4.4 SERS Detection of R6G

SERS measurements were performed on substrates immobilized for 48h using R6G as the target analyte. R6G is chosen due to its greater prevalence in SERS research[14,58,87,94,95], its ability to adsorb onto silver surfaces[14], and its large scattering cross section as a resonant Raman scatterer[14,94]. Thus R6G provides a good opportunity to characterize substrate sensitivity. Figure 11a shows the molecular structure of R6G. It is a large aromatic molecule, with many possible bond bending and stretching modes, which explains its large Raman scattering cross section. To demonstrate the SERS effect, figure 11c shows the Raman spectrum of R6G dropped on glass, on the substrate, and water on the substrate. The SERS signal of R6G at 10^{-5}M on substrate is significantly larger than the Raman signal on a glass at a concentration 5000 times larger (0.05M). The water on substrate spectrum reveals the intrinsic background of the substrate, which is due to a combination of the characteristic LSPR of the nanoparticle monolayer, and the leftover PVP and TSC adsorbed onto the silver surface from the synthesis step. Slight discoloration of the part of the substrate under the laser spot was observed after the 10s acquisition, attributed to the sintering of particles due to laser heating. Table 3 shows the peak assignments for the various peaks observed in the SERS spectrum, and their corresponding EFs using d_p = 45nm, N_s = 171μm^{-2}. α was determined to be 1.22.

Short exposure SERS spectra centered at the 609cm^{-1} peak were taken to determine the lower detection limit of the substrate. An acquisition time of 1s was used to prevent hot-spot loss due to sintering. Figure 12a shows the spectra of R6G successively diluted to using a ratio of 1:9, and 12b plots the peak height. The spectra shown represent the average of 3 acquisitions at different positions across the substrate. At and below 10^{-9}M, some acquisitions did not show a peak, indicating approach into the single molecule regime[96]. Only acquisitions which yielded a peak were included in the analysis. The 609cm^{-1} band was identifiable down to a detection limit of 10^{-10}M (0.4ppb), with roughly one tenth of the acquisitions yielding a positive result at this level. Spatial variability in signal strength was less than 15% (by peak height).

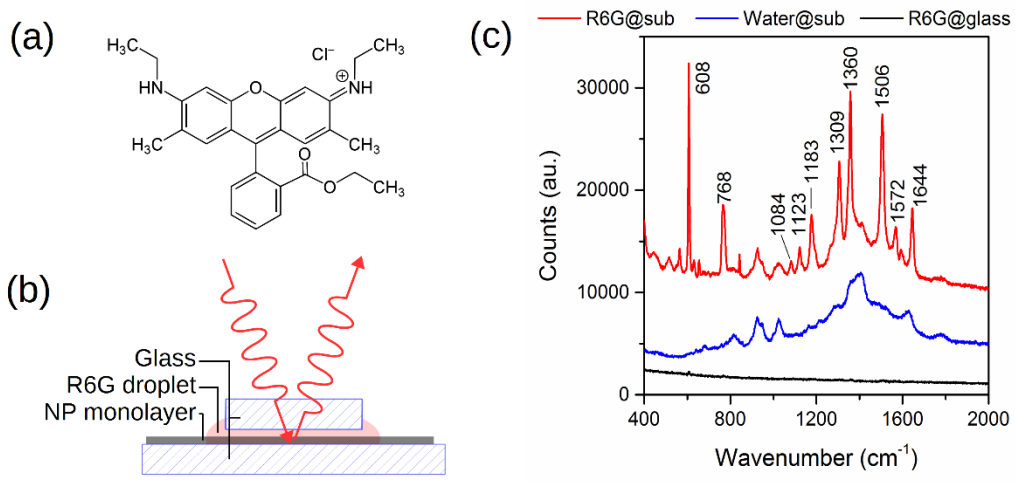

Figure 11. (a) Molecular structure of R6G. (b) Depiction of analyte smear method using a glass cover slip. By focusing the objective lens on the nanoparticle surface, the laser focused in between the cover slip and substrate, and the SERS scattering volume is sandwiched within. (c) Raman spectra of R6G 0.05M on glass (black), water on substrate (blue), and R6G 10^{-5}M on substrate (red).

Peak center (cm^{-1})	Assignment	EF'
608	C-C-C ring in-plane bend	4.5×10^5
768	C-H out-of-plane bend	3.1×10^5
1084		-
1123	C-H in-plane bend	-
1183		1.1×10^6
1309	Aromatic C-C stretch	5.0×10^5
1360		7.0×10^5
1506		5.4×10^5
1572		-
1644		7.0×10^5

Table 3. Table of peak assignments for R6G[14], and corresponding EF' for each peak. Some peaks were unable to be resolved from the background noise in the normal Raman spectra due to their low intensities, and are therefore absent in the table.

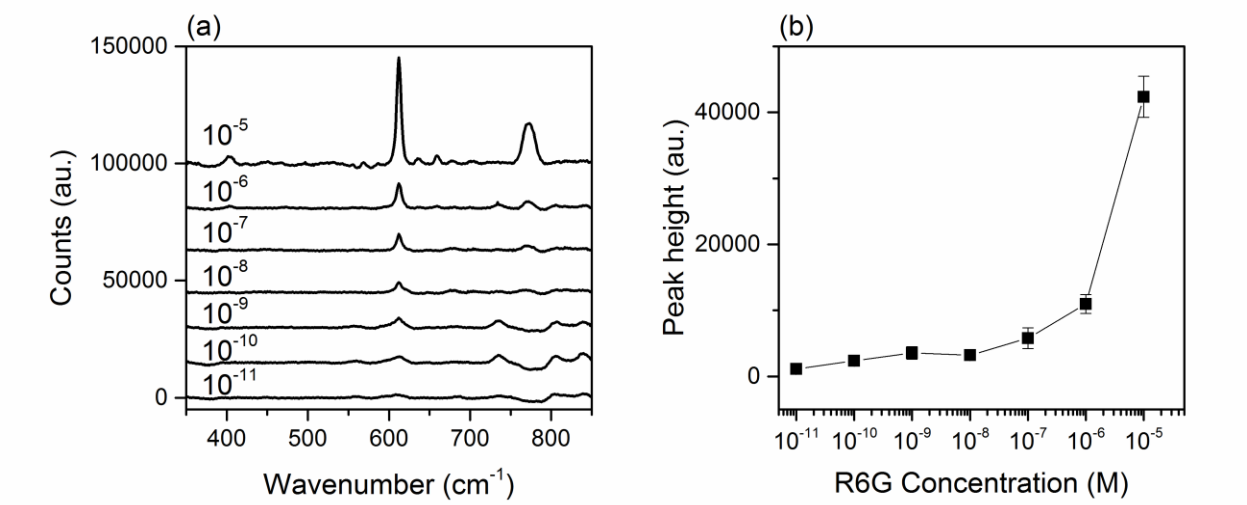

Figure 12. Short acquisition time Raman measurements of the 609cm^{-1} R6G peak at various concentrations. Figure (a) shows the spectra around 609cm^{-1} for various concentrations, and (b) plots the peak height dependence on concentration on a logarithmic scale. Error bars represent standard deviation across 4 measurements.

3.5 Discussion

3.5.1 Nanoparticle Synthesis

The synthesis of monodisperse silver nanoparticles presented several unique challenges not discussed in the results section. Many of these challenges were resolved by experimental trial and error with each iteration of synthesis. For example, excess ammonium is inevitable when making a solution of $Ag(NH_3)_2^+$, which dissolves a small amount of silver seed upon mixing. Slight variations from human error in mixing leads to the dissolution of varying amounts of seed, leading to varying final particle sizes. Additionally, it was observed that the use of ultra pure water obtained from an alternate filtration system resulted in a change in particle dispersity. Furthermore, the use of seeds greater than 2 weeks old resulted in a dark opaque purple colloid which was found to have very high polydispersity with deviation of ~50%. Some factors that were uncontrolled for include temperature, pH, and atmospheric conditions, all of which have been reported to affect nanoparticle properties[97].

In this study, we used PVP and TSC as particle stabilizing agents. The majority of silver nanoparticle syntheses include TSC as a stabilizing agent, often in conjunction with PVP, and

surfactant-free silver nanoparticles are rare[17]. PVP has been shown to shield Ag NPs from changes chloride, sulfate, and nitrate environmental changes where TSC and polyethylene glycol failed[98]. It more strongly adsorbs onto the Ag surface than TSC, and steric repulsion of the polymer chains prevents agglomeration in solution[99]. PVP has also been shown to preferentially adsorb onto the {100} facets of the silver lattice[64] which is exploited to produce nanowire, nanocube, and other exotic structures. By using an excess of surfactant, surface specific adsorption is overwhelmed and the result is spherically shaped particles. Here we use a mixture of TSC and PVP, where the molar ratio of TSC to PVP is 9:1. The result is spherically shaped particles that are not entirely covered by the strongly adsorbing PVP so as to provide surface sites for analyte adsorption.

In particle aggregate based substrates, monodispersity is not a necessary requirement for observing single molecule SERS, and highly disparate shaped nanoparticles have been demonstrated to exhibit single molecule sensitivity[100]. Nonetheless, polydispersity lowers the reproducibility of the location, density, and nature of hot-spot containing aggregates. This limitation is an issue in the large scale fabrication of reproducible SERS substrates. Figures 9 and 10 were produced using a newer batch of nanoparticles from all the other measurements. This batch was notably more polydisperse than presented in figure 7, with a standard deviation of ~14nm (compared to ~7nm). This was due to the fact that the synthesis was performed a week after the previous one, seeds had been aged for an extra week. This was advantageous for revealing the competition in immobilization between different particle sizes, illustrated in figure 10b, but is ultimately detrimental to SERS signal reproducibility.

3.5.2 Substrate Fabrication

Nanoparticle immobilization was achieved using APTES, which integrates into the silica surface matrix and provides surface of densely packed amine groups. The quality of the APTES functionalisation must be carefully controlled, as defects would lead to non-uniformity of the resultant nanoparticle film, at a scale visible only with electron microscopy. In fact, it was observed that 2h of functionalisation sometimes caused the formation of vertically stacked nanoparticle aggregates, which are difficult to characterize. This is likely due to buildup of multilayers of APTES, causing uneven adsorption and an increase in surface charge[88]. Taken to

the extreme, 24h of functionalisation caused darkening of the nanoparticle solution upon immersion. In this case, it is hypothesized that an excess of APTES molecules leached into the nanoparticle solution and caused agglomeration, due to the molecules surfactant-like nature. The color change supports this this theory, as darker colloids indicate larger particle sizes, or in this case, agglomerates. A functionalisation time of 1h has been reported to give the smoothest monolayer[88] with the greatest charge density[59], and was therefore used in this study.

The quality of synthesis and slide functionalization ultimately determined the quality of the silver nanoparticle monolayer. An aesthetic, uniform monolayer is not a prerequisite for SERS, as the only feature necessary for strong SERS enhancements to occur is an abundance of hot-spots. Indeed it has been reported that multiple iterations of particle deposition results in multilayered substrates showing greater sensitivity with each deposition, however the same study also shows a large spatial signal variability with a long tail distribution[20]. This would be impractical for quantitative detection applications, such glucose sensing[48]. The adoption of self-assembly based substrates into integrated SERS detection systems necessarily requires reproducible spot-to-spot signals, and substrates.

3.5.2 SERS

In calculating EFs, a major assumption made was that the height of the scattering volume is defined by the nanoparticle height. In reality, the gap between the substrate and cover slip is likely to be larger when a liquid is present. The adhesive force between the liquid and two surfaces sucks in liquid and exerts a pressure upon the two surfaces, akin to a horizontal capillary pressure, which is sufficient to support the weight of the cover slip. This would lead to underestimated EFs, as the amount of molecules contributing to the signal in the normal Raman case are underestimated.

It is important to note that these EFs represent a spatially averaged EF. Typically, EFs on the order of 10^8 to 10^{10} are quoted as the requirement for single molecule detection[86]. Due to their highly localized nature, the distribution of EFs across the substrate is skewed, especially for low analyte concentrations. Overall EFs are on the order of 10^5 to 10^6 but local SMEFs could be much larger, and those positions likely contribute to the majority of the signal. The

electromagnetic problem of scattering off of homogeneous metal sphere clusters has been solved analytically in 3D using the Mie solution Maxwell's equations[32]. Using these results, Ru et al. solved for EF exactly in a 50nm silver nanoparticle dimer structure with a 2nm gap setup and found the spatially averaged EF to be 285 times smaller than the maximum enhancement in the middle of the dimer structure[86]. An implication of this is that a single molecule in a hot-spot can contribute as much signal as ~300 randomly positioned molecules. Thus it is likely that local SMEFs achieved on our substrate reach the necessary sensitivity for single molecule detection. The detection limit of 10^{-10}M achieved is further evidence for single molecule sensitivity as this concentration corresponds to a number density of 0.006 molecules per μm^3.

3.6 Conclusions

Silver nanoparticle monolayers were fabricated by solution based self-assembly. With APTES as the immobilizing molecule, and capping agents PVP and citrate, we obtained a surface characterized by particle clusters spaced evenly apart in a monolayer. These substrates were then applied towards SERS, and evidence suggests single molecule sensitivity. Therefore, we conclude the following:

- Solution based self-assembly is a successful method to produce highly dense and uniform silver nanoparticle coatings which can be used as a SERS substrate with very good sensitivity towards the dye molecule R6G
- With 45nm diameter particles, the average saturated surface density was ~170μm^{-2} with standard deviation of 3%, and the average hot-spot density was ~150μm^{-2} with a standard deviation of 3%. This low variance is obtained when analyzing images of 2.16μm^2, so uniformity is not an issue when using laser spots of equivalent or larger area.
- The spatially averaged SERS enhancement factor for R6G reached 10^6, and detection limit for R6G was found to be of 10^{-10}M or 0.4ppb. This ultra-low concentration, combined with sufficient EF likely indicates single molecule sensitivity.

Chapter 4: Plasmonic Manipulation of Silver Nanoparticle Monolayers

4.1. Summary

In this chapter, plasmonic manipulation of silver nanoparticle monolayers is studied using a pre-fabrication method by particle size tuning and post-fabrication method by thermal treatment. Particle sizes from 35nm to 65nm were synthesized and deposited in a monolayer. The monolayer properties are studied as a function of particle size. We find that the SERS performance of the substrate increases with particle size within this range, despite the loss in surface density, and verify the result with electromagnetic simulations. We then study the effect of thermal treatment on the substrates. The morphological changes are correlated with the changes in the LSPR profile of the substrates, and their SERS performance is evaluated. Generally, thermal treatment causes a decrease in SERS performance, but a recovery of the SERS signal is observed at 400°C treatment and beyond, owing to the decomposition of silver oxides.

4.2 Introduction

The localized surface plasmon resonance is the main phenomenon exploited for use in plasmonic applications. The enhanced local electromagnetic fields due to the LSPR are responsible for the large signals observed in surface enhanced Raman spectroscopy[15] or metal enhanced fluorescence[13]. The absorptive properties of an LSPR active layer can also be used in intrinsic plasmonic applications such as light trapping layers[9] and backscattering layers[43] in solar cells. All of the applications depend on the LSPR profile, and the ability to tune the LSPR is useful for application specific optimization. The LSPR of a nanoparticle monolayer ultimately depends on the morphology of the individual nanostructures that make up the coating. Therefore, alteration of the LSPR is done through manipulation of the nanostructures, at the fabrication stage, or via a post fabrication treatment.

In SERS, it is well known that correlation of the LSPR maximum resonance with both the excitation wavelength and the target Raman band leads to improved signal-to-noise ratio and

increased enhancement factors[25]. The largest SERS EFs are achieved when LSPR maximum wavelength falls within a ~120nm window that includes the excitation wavelength and the Raman shifted photons wavelength[25]. The shape of nanostructures used also plays a role, as sharp corners tend to produce extremely strong local EFs through the lightning rod effect[15]. For example, Rycenga et al. compared the differences in SERS enhancement factors between nanospheres and nanocubes, and found a sharp increase in EF with cubes oriented corner to corner when the laser is polarized along the dimer axis.

In this study, we alter silver nanoparticle monolayer substrate morphology by changing particle size, and applying a thermal treatment. In the case of silver nanospheres, increasing particle size is known to produce a redshift in LSPR[33]. This can be used to increase absorbance at a given excitation wavelength. According to the results of reference [25], this ought to increase SERS EFs due to stronger LSPR coupling to the incident light. Conversely, the maximum particle coverage and surface density has an inverse dependence on particle diameter, which may be detrimental to SERS signals due to the loss of hot-spots. These two conflicting effects will both occur on the substrate, therefore it is necessary to obtain experimental data to determine the final effect of particle size on SERS performance. Thermal treatment also has the ability to alter the LSPR, as particle sintering changes the morphology of the monolayer[101]. Using these two methods, the changes in LSPR are characterized using UV/vis absorption spectroscopy, and the SERS performance is evaluated.

4.3 Materials and Methods

4.3.1 Materials

Materials used for the synthesis of nanoparticles and monolayer substrates were identical to those listen in section 3.3.1. For the thermal treatment tests, SERS substrates were made according to the procedure laid out in section 3.3.4, using the nanoparticles synthesized by the procedure in section 3.3.3. These nanoparticles will hereafter be labelled NP_0.

4.3.2 Fabrication of Size Varied Silver Nanoparticle Monolayers

The same method as described in section 3.3.3 was used to make particles of varying sizes, with a change in the amounts of precursors used. By decreasing the amount of seed, keeping the amount of amine-complexed silver the same, and adjusting the amounts of TSC and PVP accordingly, larger particles were obtained. Similarly, increasing the amount of seed decreased the size of the particles.

Silver seeds were obtained using the procedure in section 3.3.2. Solutions of 0.12M $[Ag(NH_3)_2]^+$, 0.01M PVP, 0.1M TSC, and 0.1M ascorbic acid were prepared. 2mL of $[Ag(NH_3)_2]^+$ was added to 50mL of water under stirring. Knowing the amount of atomic silver in amine-complexed form (46µmol), and seed concentration ($1.1x10^{-7}$M), the amounts of seed, PVP, and TSC to be added were calculated and are summarized in table 4. Calculations were based on the assumption of homogeneous growth of seeds. Given the total volume of silver and a target diameter, the total number of nanoparticles can be calculated by division. Then amounts of PVP and TSC were scaled based on the total available nanoparticle surface area, using the ratios from the NP_0 synthesis. Appropriate volumes of the above solutions were added to the batch solution, which was then topped up to 100mL with water. Then, 3mL 0.1M ascorbic acid was slowly added dropwise every 10s. SERS substrates were made using these 5 solutions according to the procedure laid out in section 3.3.4 with a 48h immobilization time.

Notation	Seed (mL)	PVP (µmol)	TSC (µmol)	Expected diameter (nm)	*Measured diameter (nm)
NP_1	1.692	14.82	132.69	20	34.9
NP_2	0.210	7.36	65.88	40	39.5
NP_3	0.062	4.90	43.89	60	47.2
NP_4	0.026	3.68	32.91	80	56.4
NP_5	0.013	2.94	26.33	100	64.6

*Table 4. Summary of reagent amounts used in synthesis of size varied silver nanoparticles. *Measured diameter is based on SEM imaging.*

4.3.4 Thermal Treatment

A quartz tube furnace was heated to the specified temperature under a flow of 99.99% argon gas. NP_0 monolayer substrates were placed in the middle of the quartz tube for 15 minutes. Upon removal, the substrates were gently placed at the edge of the tube and allowed to cool for 1 minute to prevent thermal stress cracking.

4.3.5 Instrumentation and Characterization Methods

All instrumentation and characterization methods were identical to those outlined in section 3.3.5. Finite element modelling of nanoparticle LSPR was performed using COMSOL Multiphysics 5.0 using the electromagnetic waves module. The local dielectric function of silver was retrieved from reference [34].

4.4 Results

4.4.1 Effect of Particle Size on Solution and Substrate Characteristics

4.4.1.1 Visual Appearance

Tuning of the nanoparticle size in nanoparticle monolayers is achieved through the synthesis. Upon addition of the ascorbic acid catalyst, the color changes observed in the NP_5 solution were as follows: transparent gold, to transparent orange, to semi-opaque ochre. The color changes observed in the smaller nanoparticle solutions followed the same color evolution path, but stopped midway with complete consumption of the silver diamine. The NP_4 and NP_5 solutions would sediment over 3 or more days, but stirring brought the solution back to its original color, indicating no physical changes to the nanoparticles and good stability. Figure 13 shows photographs of the solutions and the corresponding substrates produced. Substrates varied from green-blue for smaller particles to brown for larger particles, with a continuous gradient in between.

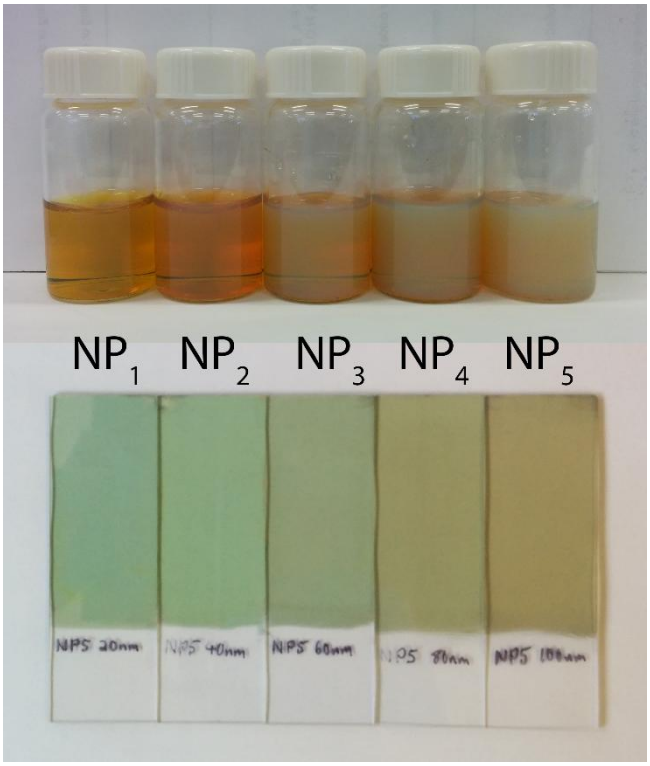

Figure 13. Photographs of size varied nanoparticle solutions and substrates.

4.4.1.2 Morphology

SEM imaging was used to inspect the substrate morphology. Figure 14 shows the images and corresponding size distributions. As the particle size increases, the solutions become more polydisperse, with the standard deviation in size increasing from 7% for NP_1 up to 23% for NP_4. While the amounts of TSC and PVP added were scaled with final surface coverage, they affect the initial solution conditions during the nucleation and early growth stages, which are the same for all batches. Thus the ratio of surfactant to seed surface area is much higher for the NP_5 batch, compared to the NP_1 since the amount of seed was reduced while the amount of surfactant was increased. This dramatically altered the solution ionic strength during the initial stages of growth, and resulted in a polydisperse solution. Nonetheless, we were still able to achieve increasing average particle sizes which could be used to elucidate the size dependent properties of SERS.

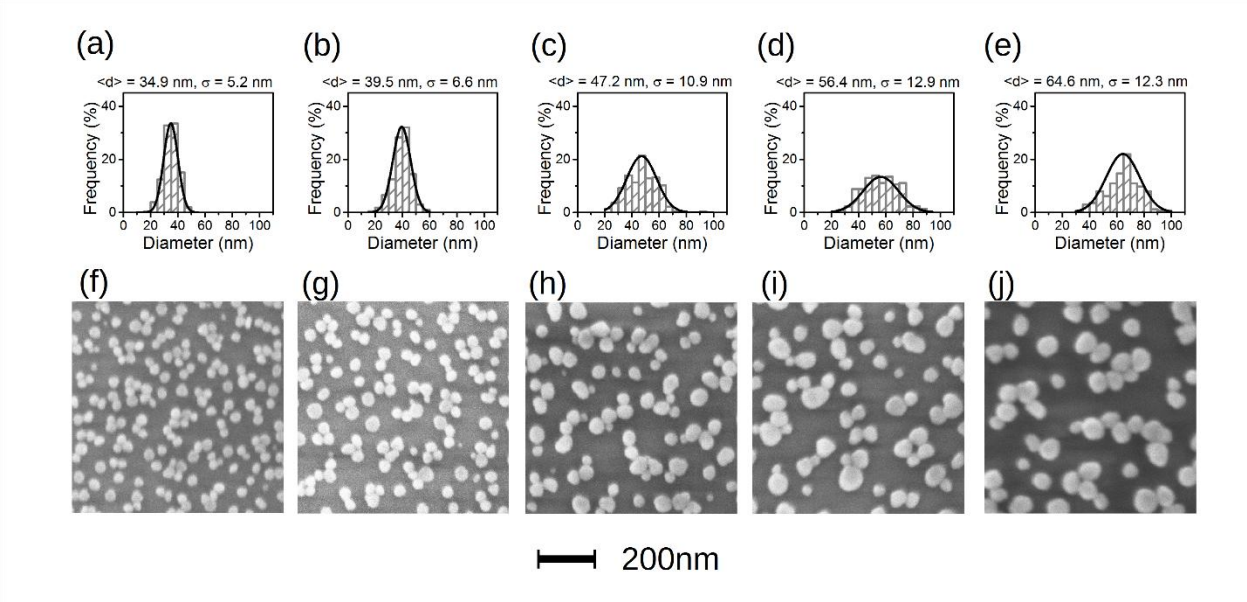

Figure 14. Composite of (a-e) size distribution histograms for NP_1 to NP_5 substrates, and (f-j) corresponding SEM images. <d> denotes average diameter, and σ is the standard deviation. Scale bar shown is applicable to all images.

By using APTES as a supporting layer with 48h deposition time, maximum surface density is attained on all substrates. The random sequential adsorption (RSA) model allows one to theoretically predict the maximum coverage of particles interacting through a screened Coulomb potential for various shapes and sizes. For spherical particles, maximum coverage θ_M can be approximated by[17]

$$\theta_M = \theta_0 \left(1 + \frac{2h}{d_p}\right)^{-2} \tag{13}$$

where θ_0 is the maximum coverage for non-interacting particles (0.547 for spheres), h is the interaction range, and d_p is the particle diameter. Combining this with equation (11), the predicted surface density at saturation is

$$N_s = \frac{4\theta_0}{\pi(d_p^2 + 2h)} \tag{14}$$

A plot of N_s versus d_p is shown in figure 15. Using average diameter, and assuming a constant interaction range, this data was fit to the RSA model using equation (14). Using a least squares fitting algorithm, h is predicted to be 17.2nm, with $R^2 = 0.86$.

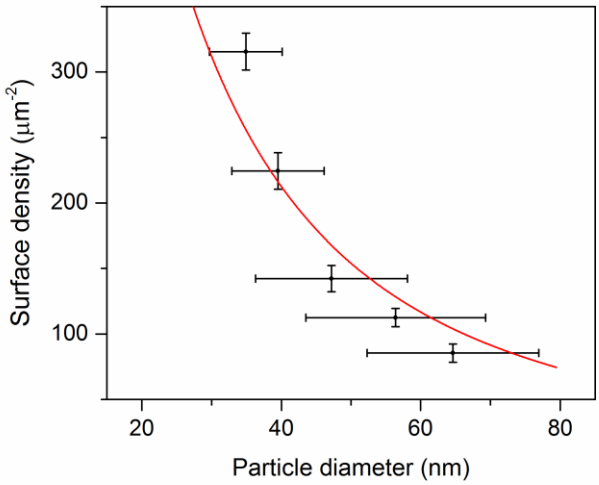

Figure 15. Dependence of the nanoparticle monolayer density on nanoparticle diameter. For surface densities, nanoparticles were counted over 3 SEM images of dimensions 1.2μm x 0.8μm, and averaged. The red curve was generated by a fit to the RSA model for nanoparticle maximum coverage. The error bars represent standard deviation.

4.4.1.3 Optical Absorbance

UV/vis absorbance spectra were taken to characterize the localized surface plasmon resonance of the size varied nanoparticle solutions and substrates, plotted in figure 16. The solution spectra show a primary LSPR peak from 400nm to 440nm characteristic of individual spherical nanoparticle absorption. Generally, a redshift and broadening is observed with the solution spectra, in accordance with the increasing size and polydispersity observed in the SEM images[89]. The exception to this is the NP_1 solution, where the LSPR peak occurs at 429nm. This redder peak is likely due to plasmon coupling to surrounding NPs due to the higher concentration of NPs[102], emphasized by the deficiency of surfactants compared to the other solutions. A blueshift of the overall spectrum occurs from solution to substrate, because of the refractive index change from water to air[18]. The substrates show a double peak feature at 375nm, due to depolarization of the primary LSPR mode[33], and a long wavelength absorption feature at 600nm to 700nm, which is characteristic of LSPR coupling for dimers and higher order

aggregates[18,91]. As expected, this second feature redshifts with increasing particle size. The feature at ~375nm follows the same trend as the solution spectra, and an increase in absorption is observed with increasing size despite the lower particle coverage.

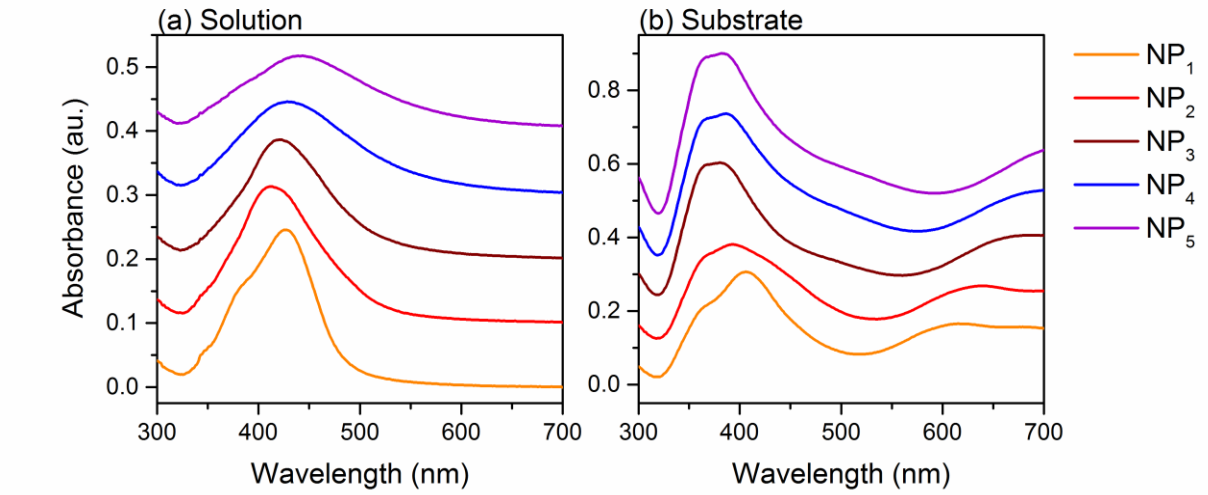

Figure 16. UV/vis absorption spectra of NP_1 to NP_5 solutions and substrates. Solutions were diluted 1:19 from the original, while substrates were taken as is. Solution spectra were relative to water, and substrate spectra were relative to clear glass. All spectra are stacked with a 0.1 absorbance offset.

4.4.2 Effect of Particle Size on SERS

The size varied substrates were used for SERS with R6G at a concentration of 10^{-5}M as the target analyte to elucidate the effect of particle size on SERS sensitivity. Using this high concentration ensures the adsorption of R6G on the silver surface is in equilibrium, and no signal blinking occurs. Refer to section 3.4.4 and figure 11 for initial analysis on the full spectrum of R6G. The Raman bands at 608, 768, 1183, and 1644 cm^{-1} were chosen for analysis, because the substrate intrinsic background is not very intense in their proximity. The particle size dependence of the SERS is shown in figure 17. An increasing trend in peak height is seen in figure 17a, consistent with the increasing strength of the substrate LSPR, and despite the decrease in surface density. This result is best explained using enhancement factors, which accounts for the drop in surface density. EFs are calculated using equation (9), and plotted in figure 17b. Generally EF also increases with particle size, where the increase goes as high as 2 orders of magnitude for some peaks. Since it is the local hot-spots which contribute the majority of the signal from a

SERS substrate[86], the increase in enhancement factor overtakes the loss of hot-spots under the Raman excitation due to the loss in surface density, and an increase in peak height is observed.

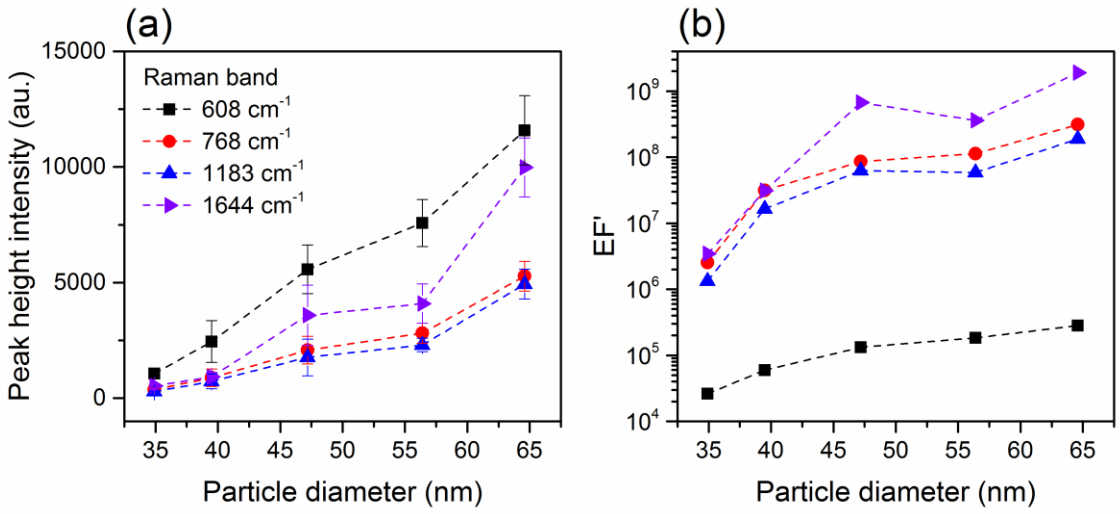

Figure 17. The effect of particle size on SERS activity. (a) Plot of peak heights of selected Raman bands using R6G 10^{-5}M on the size varied nanoparticle substrates. Error bar indicates standard deviation across 4 acquisitions. (b) EFs of the same Raman bands versus particle diameter, calculated using equation (9).

In order to verify our results, finite element modelling in 3D was used to compute the size dependence of the LSPR in a single particle, and dimer configuration. An incident Gaussian beam excitation is plugged into Maxwell's equations, and the scattered field is solved for. To visualize the LSPR, the electric field norm is computed according to the equation

$$|E| = (\vec{\mathbf{E}} \cdot \vec{\mathbf{E}})^{1/2} \tag{15}$$

Figure 18 plots a planar cross section of the electric field norm in the case of 633nm excitation and 50nm diameter particles. When in a dimer, a hot-spot forms in the space between particles, and the electric field norm is ~15x stronger than the incident power. Without the dimer, the strongest site on the particle surface is only ~3.5x stronger. While this still represents an enhancement, the SERS enhancement factor can be approximated by $|E/E_0|^4$, since intensity is proportional to E^2 and the enhancement occurs twice: on incidence, and upon scattering[86]. This 4^{th} power is the source of the dramatic scaling of EF with electric field strength observed in SERS.

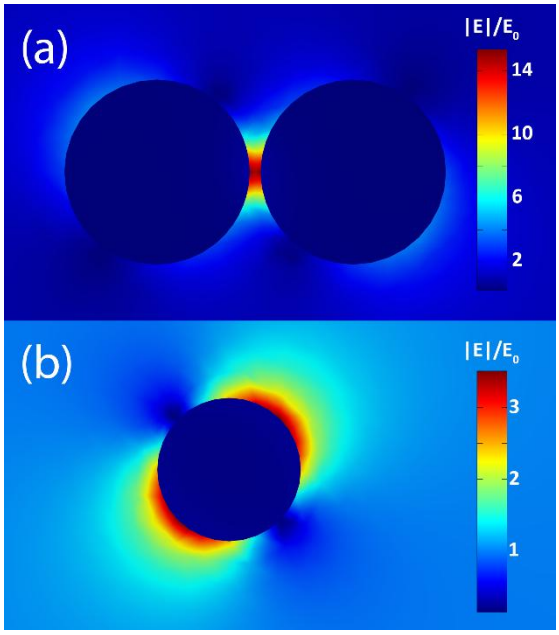

Figure 18. Visualization of the LSPR for (a) a 50nm silver nanoparticle dimer with a 2nm gap and (b) an isolated 50nm particle. The electric field norm is plotted on the z = 0 plane, giving a cross section through the middle of the particles. Incident excitation is a Gaussian beam of wavelength 633nm, beam waist diameter 3µm, and E_0 = 1V/m.

A parametric sweep of particle size, gap width, and wavelength was performed, and the resulting EFs are calculated according to $|E/E_0|^4$ and plotted in figure 19a. Electric field norms were taken at the center of the gap along the dimer axis. For comparison the maximum EF on the surface of an individual nanoparticle is shown in figure 19b. EFs for dimers are dramatically greater than individual particles, reaching values several orders of magnitude greater. Generally, EFs increase to a peak as particle size increases, and then drop by an order of magnitude. EFs are greater overall with a smaller gap, and peak earlier with shorter wavelength excitation, as expected. A secondary peak occurs due to the emergence of quadrupole resonance modes in larger particles[33]. Within the range of particle sizes used experimentally in this study, with a 633nm excitation, in all cases the EF monotonically increases. Additionally, the computed EFs are on the order of 10^5 to 10^8. Thus the simulation derived EFs are in good agreement with the experimentally observed results.

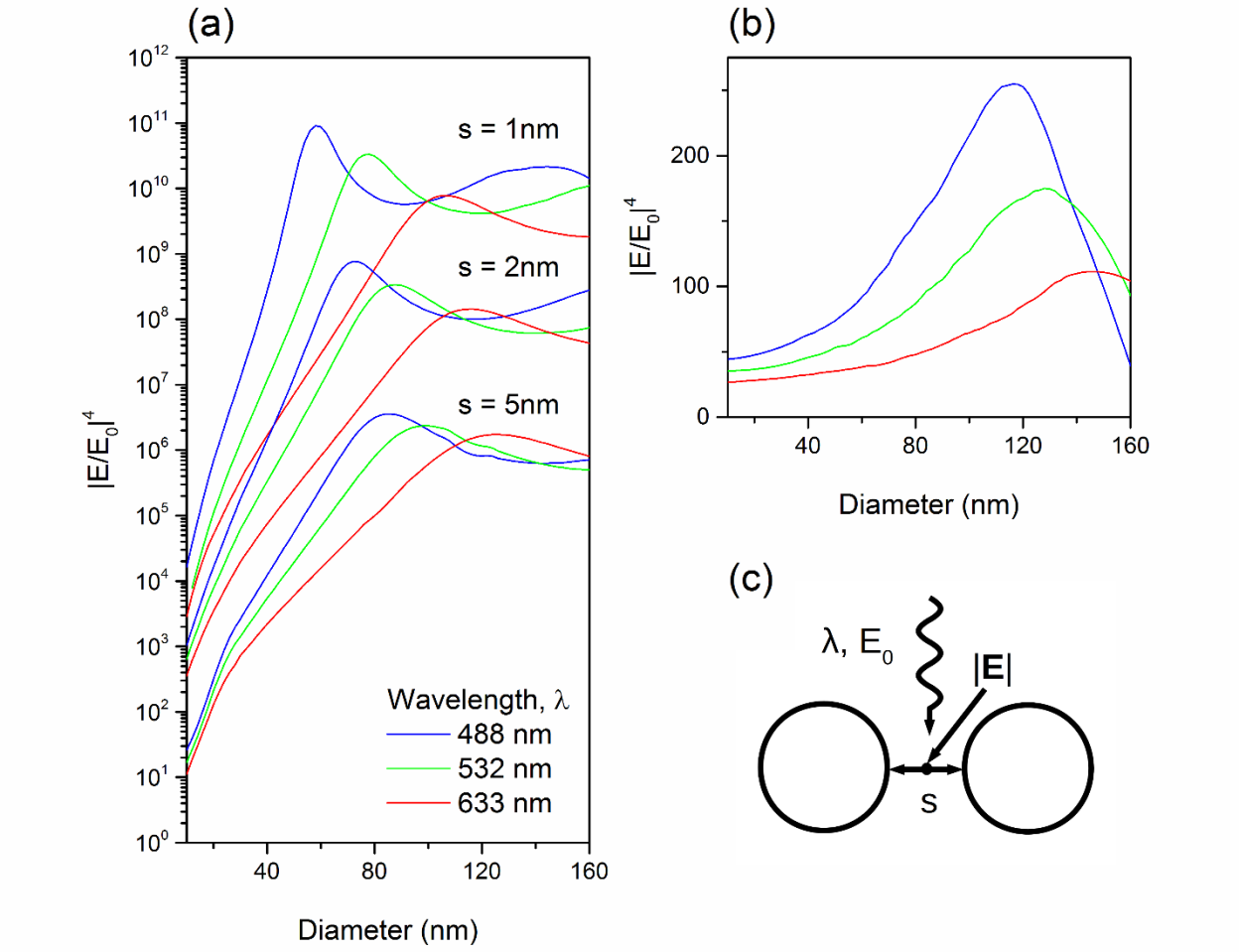

Figure 19. Plots of simulated EFs versus particle diameter (a) for a dimer configuration with various gaps, and (b) for a single particle. (c) Schematic depiction of the dimer setup showing where |E| is sampled.

4.4.3 Effect of Thermal Treatment on Substrate Characteristics

NP_0 substrates were subjected to a heat treatment from 150°C to 450°C for 15min at all temperatures. Sintering of nanoparticles was observed at 150°C, and subsequent joining is observed at 200°C forming irregular elongated structures. At 250°C and above, the joined structures continually coalesce into a circular structure, with increasing uniformity. This diffusive coalescence occurs well below the bulk melting point of silver, which is 961.8°C. Figure 20 shows the SEM images and resultant particle size histograms for applicable substrates. Particle size histograms were not included for the 150°C, 200°C, and 250°C substrates due to

particle shape irregularity. At and above 300°C, a particle size peak persists at ~35nm, corresponding to individual isolated nanoparticles that have not been consumed by the large coalesced agglomerates.

UV/vis spectra of the heat treated substrates are shown in figure 21a. The untreated substrate shows a double peak at around 375nm, consistent with previous results. A peak appears at 476nm upon heat treatment at 150°C, which blueshifts to 459nm at 200°C. The shape of these two spectra resemble that of oblate spheroids[33], indicating joining of the nanoparticles by a conductive path. The peak at 250°C occurs at 447nm, and then continually redshifts beyond this temperature. The peaks at 250°C and above are symmetrical, resembling spherical particles[55], which is consistent with the observation of coalescence into large round particles. Additionally, a narrowing of the absorbance is observed with increasing temperature, which is due to the increasing homogeneity. The progression of the tallest peak position along with the absorbance attained is plotted in figure 21b. The absorbance upon heat treatment increases as the cross section of scattering increases once the particles join. The redshift of the peaks at and above 250°C indicate growth of the coalesced particles as temperature increases.

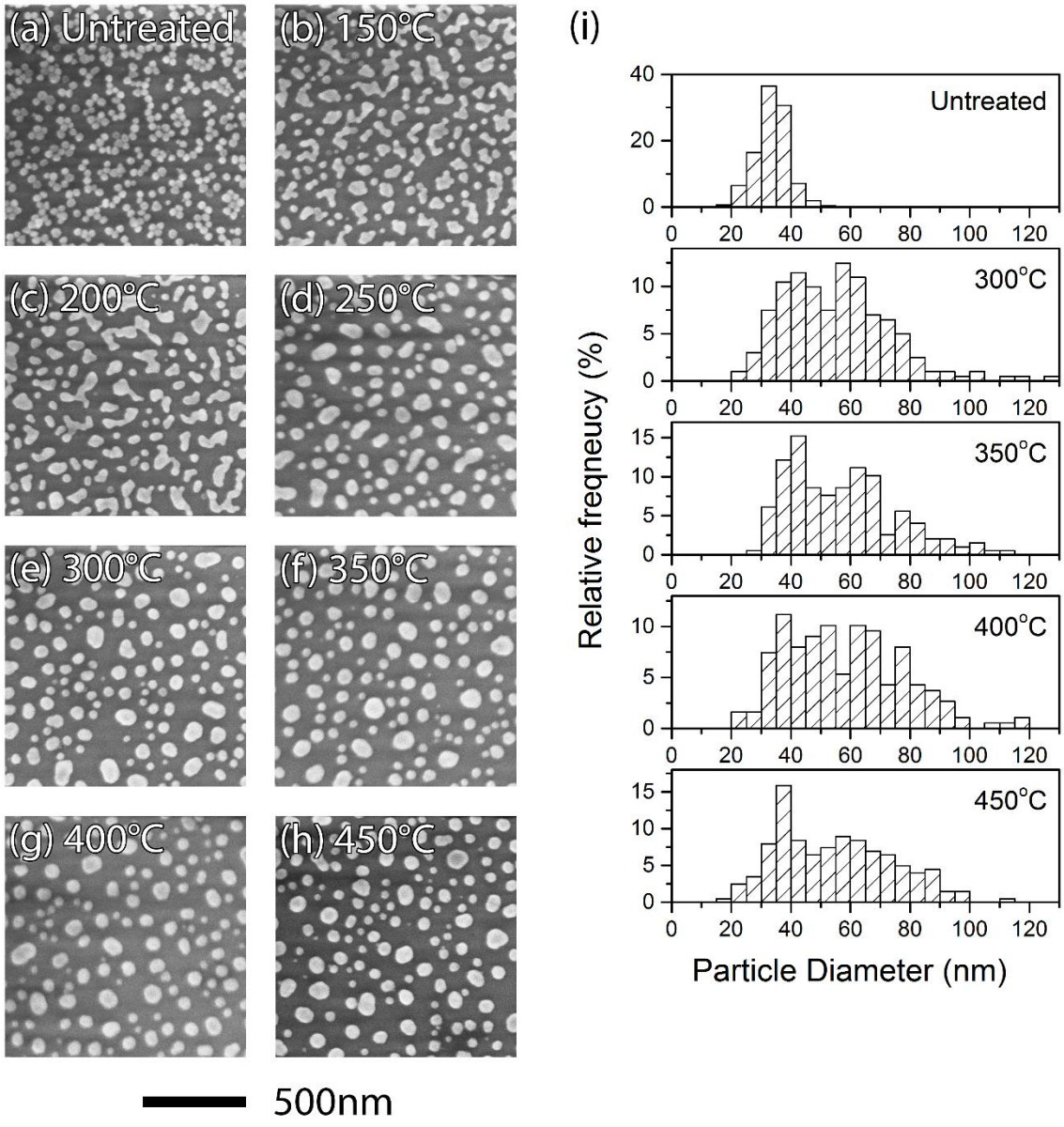

Figure 20. SEM images of (a) an untreated substrate, and (b-h) heat treated substrates. (i) Particle size histograms for various substrates. Particle sizes were measured across 2 images of 1.2µm x 1.8µm, which led to at least 400 particles included in the dataset of each histogram.

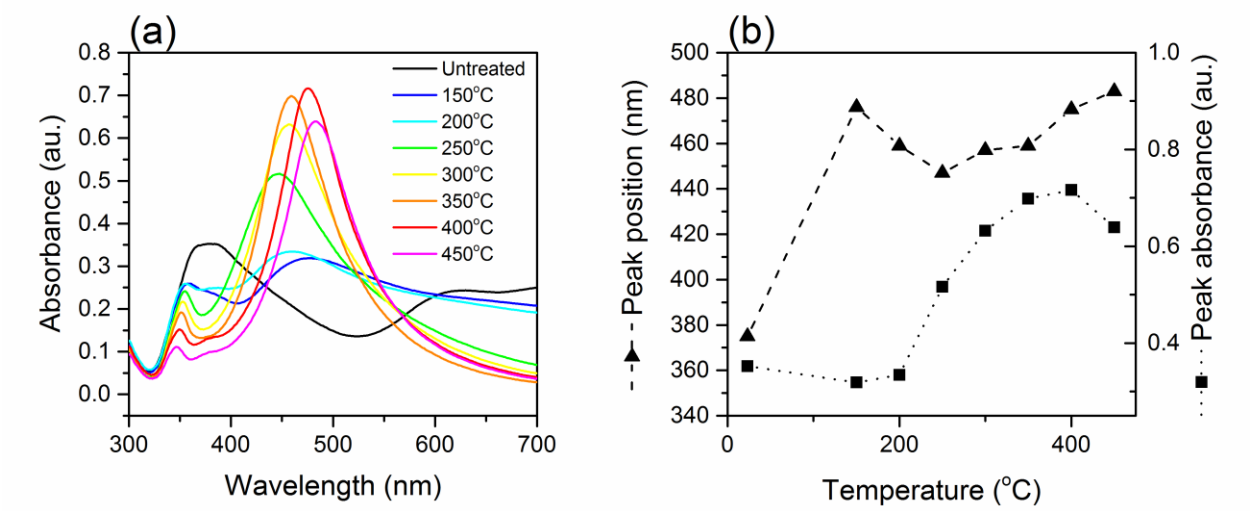

Figure 21. (a) UV/vis spectra of heat treated substrates. (b) Progression of absorption peak position and maximum attained value as a function of heat treated temperature. The untreated substrate is plotted at room temperature of 23°C.

4.4.4 Effect of Thermal Treatment on SERS

The substrates were evaluated for their SERS performance using R6G at a concentration of 10^{-5}M. Since irregular structures were present on the substrate, a characterization of the scattering volume is difficult, and instead the analytical enhancement factor is calculated. The peak heights and AEFs are plotted in figure 22. A reduction of the SERS signal is generally seen upon heat treatment, attributed to the loss of hot-spots due to particle necking. An increase in signal is observed at T = 400°C. This is likely due to the decomposition of surface silver oxide species. Silver oxide builds up over time when silver is exposed to air, leading to an insulating gap between adsorbed analyte molecules and the most active SERS sites, causing a reduction of the SERS signal[31]. Annealing at 400°C has been shown to decompose surface silver oxide species, and regenerate the crystalline silver surface, leading to recovery of SERS signals[95]. Despite the significant loss in hot-spots on the substrate, we observe an order of magnitude increase in the EF from 350°C to 400°C, with the result holding true at 450°C.

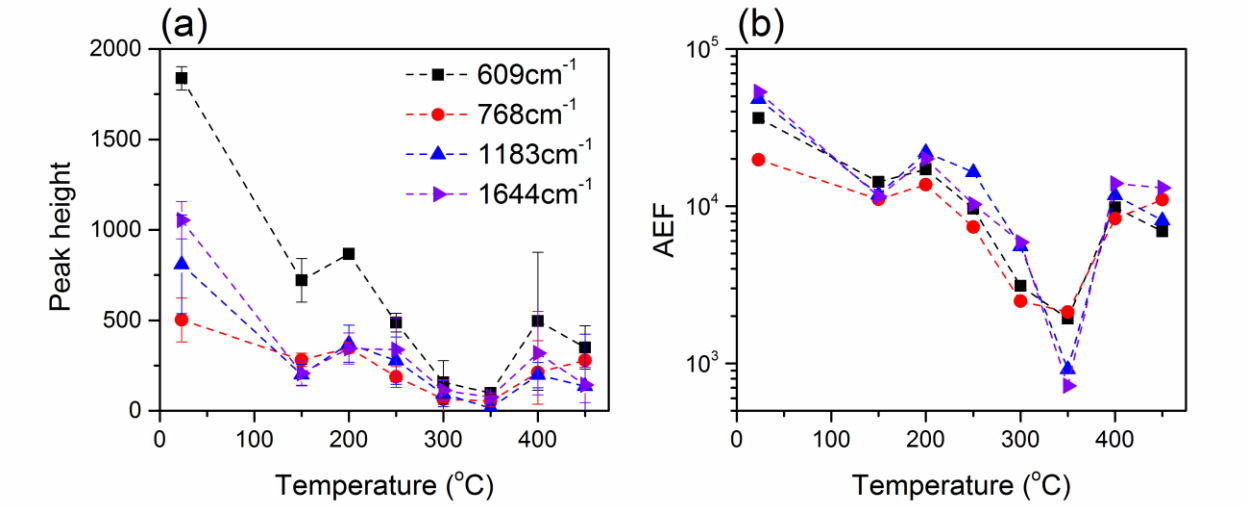

Figure 22. SERS data for thermally treated substrates. (a) Peak heights, and (b) analytical enhancement factors calculated according to equation (7). In both plots, the untreated substrate is placed at room temperature of 23°C.

4.5 Discussion

4.5.1 Optimization by Tuning Particle Size

During the study of particle size on substrate properties, a particle interaction range h was estimated to be 17.2nm, based on the assumption that it is constant in all the solutions. Since the target diameters were not met, this is an invalid assumption. An excess of surfactant is present for solutions NP_2 to NP_5, while a deficiency is expected for NP_1. TSC concentration ranged from 26μM to 1.3mM for NP_5 to NP_1, which also changes the ionic strength of each solution, however within this range, this should not significantly affect attachment efficiency during the dynamical process of agglomeration[99]. It is more likely that the interaction of surface PVP species affect the results the most, as PVP has been shown to have a charge screening effect as well provide stabilization by steric repulsion[98]. Additionally, the value of h reported is slightly lower than reported hydrodynamic diameters for various Ag NPs in solution[92,103], which can be explained by the fact that NPs immobilize in clusters. In fact, since particle agglomeration is the main mechanism of particle immobilization near saturation, the RSA model is insufficient to describe the final coverage since it is based on diffusive transport, in accordance with the results of section 3.4.2.

Increasing particle size proved to be an effective method for increasing the SERS enhancement factor. This goes against the intuition that a drop in surface density will result in a signal loss. In fact, due to stronger LSPR for a 633nm excitation, the enhancement factor gain at the SERS hot-spots overpowers the loss of the number of hot-spots in a given SERS scattering volume. The rapid increase in electromagnetic field strength observed in finite element modeling seems to support this result. This result may have its roots in a comparison of the RSA model prediction of maximum surface density to the simulated enhancement factor. The RSA model predicts a $\sim 1/d_p^2$ dependence of the surface density. This should have a linear effect on the overall SERS signal, as signals intensities originating from multiple hot-spots adds linearly. However, figure 15a shows an exponential increase in EF with d_p up until ~90nm for the 633nm excitation used.

For other applications, such as for plasmon-enhanced solar cell back scattering layers, the important feature of silver nanoparticle monolayer is its LSPR profile. We have demonstrated the redshifting of the long wavelength absorbance feature at ~600nm with increasing particle size. Also, while the absorbance double feature at 375nm does not shift, it does increase in magnitude with particle size, despite the lowering surface density. The design of solar cell backscatterers for specific illumination conditions may take these facts into consideration when choosing a particle size.

4.5.2 Optimization by Thermal Treatment

The surface morphology of untreated substrates comprises of silver nanoparticle clusters with nanometer gaps in between particles known to give rise to a significant number of SERS hot-spots. Upon thermal treatment, particle necking and diffusive coalescence eliminating the presence of these dimer based hot-spots, and causing an overall decrease in the SERS enhancement. Small enhancements are still observed owing to the intrinsic LSPR of individual nanoparticles, as shown in figure 18b. However, the EF recovers at and beyond 400°C, owing to the decomposition of Ag_2O to Ag, which regenerates binding sites and makes surfaces more active[31,95]. One important implication of this result is that this opens surface chemistry pathways for specific analyte binding. Almost all self-assembled monolayers contain surfactant species which stabilize the particle colloid and persist during monolayer formation, which makes it

difficult to functionalize the surface with protein receptors or capture layers. For example, glucose sensing with SERS requires either a capture layer of chain molecules[48], or glucose binders such as 4-mercaptophenylboronic acid. Previously, this has been only achieved on pristine silver and gold based substrates fabricated using lithographical techniques. Heat treatment can decompose the organic surfactant molecules, which breakdown above 300°C, and provide a clean silver surface for subsequent functionalization.

4.6 Conclusions

We have demonstrated the tuning of the LSPR of silver nanoparticle monolayers by altering particle size and by thermal treatment. Both of these methods alter the morphology of monolayers, and allow for controlled shifting of LSPR peaks. Specifically, the results achieved in this chapter are:

- Increasing particle size leads to a redshift of the plasmon coupled absorbance feature at ~600nm in silver nanoparticle monolayers.
- Contrary to intuition, increasing particle size does not cause a redshift the primary LSPR peak at ~375nm, but does cause an increase in absorbance magnitude of this peak.
- Increasing particle size up to 65nm leads to an increase in EF, which is more prominent than the decrease in hot-spot density, and therefore leads to increased SERS strength.
- Thermal treatment moves the substrate LSPR profile back and forth, and we have correlated the changes in LSPR with morphological changes on the substrate.
- Thermal treatment leads to SERS signal loss due to joining and coalescence of the nanoparticles. However, treatment at 400°C and beyond leads to decomposition of surface silver oxide, which recovers SERS signals and opens the pathway for engineering surface chemistries.

Chapter 5: Conclusions and Recommendations

5.1 Summary

This thesis presents new findings in the field of nanotechnology, particularly in the application of plasmonic silver nanoparticle monolayers towards sensing through SERS. Chapter 2 was a literature review which established the background of SERS, and the current state of substrate technology was established. Following this, chapter 3 described the development of a method for fabricating silver nanoparticle monolayers using self-assembly techniques. This substrate was successful for SERS, as evidence for single molecule detection was found. Using the same technology, chapter 4 presented experimental studies on some of the morphological aspects of silver nanoparticle monolayers, and their effect on SERS sensitivity. The physical effects of particle size and thermal treatment were characterized, and those morphological changes were correlated with observed LSPR changes and SERS enhancements. In summary, this thesis establishes a protocol for the development of a low-cost and scalable SERS substrate, and provides insight into the SERS and LSPR behavior of this type of substrate under certain morphological changes.

5.2 Conclusions

In conclusion, self-assembly is a favorable approach to making silver nanoparticle monolayer SERS substrates with single molecule sensitivity. This method produces a surface characterized by a single layer of nanoparticle clusters, which contain a high density of nanoparticle dimers leading to high SERS sensitivity. Single molecule sensitivity is likely achieved with the dye molecule R6G. Particle size tuning can be used to optimize these substrates for a given Raman excitation wavelength, and thermal treatment can be advantageous in applications requiring a clean silver surface, particularly when additional chemical functionalization is required. Specifically, the following results were achieved:

1. The average saturated surface density for nanoparticle monolayers consisting of 45nm PVP and citrate capped particles was found to be $171\pm5\mu m^{-2}$ and the average hot-spot density was $151\pm5\mu m^{-2}$ over areas of $2.16\mu m^{-2}$. Thus substrates are uniform over micron

distances, allowing for good signal reproducibility using micron or larger sized beam widths.

2. Using R6G as a target analyte in SERS, the largest enhancement factor of this substrate was determined to be ~10^6 for the 1183cm^{-1} peak. The lower detection limit for R6G was found to be 10^{-10}M. This low concentration plus sufficient EF is evidence for single molecule sensitivity.
3. Increasing particle size from 35nm to 65nm greatly increases the LSPR coupling to light at 633nm, leading to an increase in EF which outweighs the decrease in hot-spot density. This leads to an overall increase in SERS signal strength. This increase should continue up to ~100nm for 633nm light. Therefore, SERS substrates may be optimized by choosing the correct particle size for a given wavelength of excitation.
4. Thermal treatment causes particle joining and coalescence which both diminishes the SERS hot-spots found in between nanoparticle dimers, as well as decreases the surface density of nanostructures. This leads to a loss in SERS signal. However, above 400°C, signal recovery occurs due to the decomposition of surface silver oxide species. While this does not recover the original level of EF, removal of surfactants and regeneration of the silver surface opens chemical pathways for functionalization with binding agents, which allows the detection of non-adsorbing species.
5. Both particle size tuning and thermal treatment lead to controllable changes in the LSPR profile of silver nanoparticle monolayers, which can be applied towards integration in solar cells.

5.3 Recommendations for Future Work

Based on the results of this research, several avenues of research are recommended in continuation or branching of the current work:

1. Test the stability and robustness of the substrates by aging in air and seeing the effects on the substrate. While an attempt was made to use all substrates freshly within 1-2hrs of fabrication, a short-time signal decay may be a confounding factor in the data.
2. Expand the particle size data range by improving on the synthesis method to produce larger particles, at 100nm or greater. Using a 488nm excitation, a drop in signal should be

observed at this size range according to the simulation results of section 4.4.2. This would verify the simulations, which can then be used to definitively say which particle size is the best.

3. Perform a post heat treatment surface functionalization. SPR spectroscopy can be used to monitor the changes in LSPR, and study the binding kinetics of the chosen molecule. This can then be used to study protein binding interactions on the functionalized substrate, or to bind and detect molecules that do not regularly immobilize on the substrate.
4. Perform SERS detection of different analytes, and quantify the signals with concentration. This would be useful for water treatment assays, and provide a quick low-cost detection or verification platform for certain molecules. Some examples include pesticides, dyes, and estrogenic compounds.

References

[1] B. Nowack, H. F. Krug, M. Height, *Environmental Science & Technology* **2011**, *45*, 1177–1183.

[2] Shahid-ul-Islam, B. S. Butola, F. Mohammad, *RSC Advances* **2016**, *6*, 44232–44247.

[3] J.-B. Ricco, *Journal of Vascular Surgery* **2006**, *44*, 339–346.

[4] R. J. Chimentao, I. Kirm, F. Medina, X. Rodriguez, Y. Cesteros, P. Salagre, J. E. Sueiras, *Chemical Communications* **2004**, 846–847.

[5] X.-Y. Dong, Z.-W. Gao, K.-F. Yang, W.-Q. Zhang, L.-W. Xu, *Catalysis Science and Technology* **2015**, *5*, 2554–2574.

[6] V. K. Rao, K. V. Abhinav, P. S. Karthik, S. P. Singh, *RSC Advances* **2015**, *5*, 77760–77790.

[7] H. Alarifi, A. Hu, M. Yavuz, Y. N. Zhou, *Journal of Electronic Materials* **2011**, *40*, 1394–1402.

[8] J. Yu, G. Dai, B. Huang, *The Journal of Physical Chemistry C* **2009**, *113*, 16394–16401.

[9] H. Tan, R. Santbergen, A. H. M. Smets, M. Zeman, *Nano Letters* **2012**, *12*, 4070–4076.

[10] A. P. Kulkarni, K. M. Noone, K. Munechika, S. R. Guyer, D. S. Ginger, *Nano Letters* **2010**, *10*, 1501–1505.

[11] M. Wang, C. Sun, L. Wang, X. Ji, Y. Bai, T. Li, J. Li, *Journal of Pharmaceutical and Biomedical Analysis* **2003**, *33*, 1117–1125.

[12] A. M. Schrand, L. K. Braydich-Stolle, J. J. Schlager, L. Dai, S. M. Hussain, *Nanotechnology* **2008**, *19*, 235104.

[13] K. Aslan, Z. Leonenko, J. R. Lakowicz, C. D. Geddes, *Journal of Fluorescence* **2005**, *15*, 643–654.

[14] P. Hildebrandt, M. Stockburger, *The Journal of Physical Chemistry* **1984**, *88*, 5935–5944.

[15] P. L. Stiles, J. A. Dieringer, N. C. Shah, R. P. V. Duyne, *Annual Review of Analytical Chemistry* **2008**, *1*, 601–626.

[16] C. M. Cobley, S. E. Skrabalak, D. J. Campbell, Y. Xia, *Plasmonics* **2009**, *4*, 171–179.

[17] M. Oćwieja, Z. Adamczyk, M. Morga, K. Kubiak, *Advances in Colloid and Interface Science* **2015**, *222*, 530–563.

[18] Paul J. G. Goulet, J. David S. dos Santos, Ramón A. Alvarez-Puebla, J. Osvaldo N. Oliveira, R. F. Aroca, *Langmuir* **2005**, *21*, 5576–5581.

[19] Robin M. Bright, Michael D. Musick, and M. J. Natan, *Langmuir* **1998**, *14*, 5695–5701.

[20] M. Fan, A. G. Brolo, *Physical Chemistry Chemical Physics* **2009**, *11*, 7381–7389.

[21] S. Zhu, C. Fan, J. Wang, J. He, E. Liang, *Optical Review* **2013**, *20*, 361–366.

[22] Z. Wang, L. J. Rothberg, *Applied Physics B* **2006**, *84*, 289–293.

[23] L. Wang, Y. Sun, Z. Li, *Applied Surface Science* **2015**, *325*, 242–250.

[24] Adam D. McFarland, Matthew A. Young, Jon A. Dieringer, and R. P. V. Duyne, *The Journal of Physical Chemistry B* **2005**, *109*, 11279–11285.

[25] C. L. Haynes, and R. P. V. Duyne, *The Journal of Physical Chemistry B* **2003**, *107*, 7426–7433.

[26] M. Rycenga, C. M. Cobley, J. Zeng, W. Li, C. H. Moran, Q. Zhang, D. Qin, Y. Xia, *Chemical Reviews* **2011**, *111*, 3669–3712.

[27] K. A. Willets, R. P. V. Duyne, *Annual Review of Physical Chemistry* **2007**, *58*, 267–297.

[28] Jennifer M. Brockman, Bryce P. Nelson, R. M. Corn, *Annual Review of Physical Chemistry* **2000**, *51*, 41–63.

[29] A. J. Haes, C. L. Haynes, A. D. McFarland, G. C. Schatz, R. P. Van Duyne, S. Zou, *MRS Bulletin* **2005**, *30*, 368–375.

[30] V. K. Sharma, R. A. Yngard, Y. Lin, *Advances in Colloid and Interface Science* **2009**, *145*, 83–96.

[31] Y. Han, R. Lupitskyy, T.-M. Chou, C. M. Stafford, H. Du, S. Sukhishvili, *Analytical Chemistry* **2011**, *83*, 5873–5880.

[32] J. M. Gerardy, M. Ausloos, *Physical Review B* **1982**, *25*, 4204–4229.

[33] K. Lance Kelly, Eduardo Coronado, Lin Lin Zhao, and G. C. Schatz, *The Journal of Physical Chemistry B* **2003**, *107*, 668–677.

[34] P. B. Johnson, R. W. Christy, *Physical Review B* **1972**, *6*, 4370–4379.

[35] D. E. Aspnes, A. A. Studna, *Physical Review B* **1983**, *27*, 985–1009.

[36] R. Kitamura, L. Pilon, M. Jonasz, *Applied Optics* **2007**, *46*, 8118–8133.

[37] D. K. Gramotnev, S. I. Bozhevolnyi, *Nature photonics* **2010**, *4*, 83–91.

[38] N. Fang, H. Lee, C. Sun, X. Zhang, *Science* **2005**, *308*, 534–537.

[39] V. M. Shalaev, *Nature photonics* **2007**, *1*, 41–48.

[40] D. E. Chang, A. S. Sørensen, P. R. Hemmer, M. D. Lukin, *Physical Review Letters* **2006**, *97*, 053002.

[41] D. E. Chang, A. S. Sørensen, E. A. Demler, M. D. Lukin, *Nature Physics* **2007**, *3*, 807–812.

[42] C. Joachim, J. Gimzewski, A. Aviram, *Nature* **2000**, *408*, 541–548.

[43] S. Morawiec, M. J. Mendes, S. Mirabella, F. Simone, F. Priolo, I. Crupi, *Nanotechnology* **2013**, *24*, 265601.

[44] K. Aslan, I. Gryczynski, J. Malicka, E. Matveeva, J. R. Lakowicz, C. D. Geddes, *Current Opinion in Biotechnology* **2005**, *16*, 55–62.

[45] E. C. Le Ru, P. G. Etchegoin, *MRS Bulletin* **2013**, *38*, 631–640.

[46] E. C. Le Ru, E. Blackie, M. Meyer, and P. G. Etchegoin, *The Journal of Physical Chemistry C* **2007**, *111*, 13794–13803.

[47] H. Kuramitz, K. Sugawara, M. Kawasaki, K. Hasebe, H. Nakamura, S. Tanaka, *Analytical Sciences* **1999**, *15*, 589–592.

[48] Olga Lyandres, Nilam C. Shah, Chanda Ranjit Yonzon, Joseph T. Walsh Jr., Matthew R. Glucksberg, R. P. V. Duyne, *Analytical Chemistry* **2005**, *77*, 6134–6139.

[49] X. Zhang, M. A. Young, O. Lyandres, R. P. V. Duyne, *Journal of the American Chemical Society* **2005**, *127*, 4484–4489.

[50] S. Farquharson, C. Shende, A. Sengupta, H. Huang, F. Inscore, *Pharmaceutics* **2011**, *3*, 425.

[51] James M. Sylvia, James A. Janni, J. D. Klein, and K. M. Spencer, *Analytical Chemistry* **2000**, *72*, 5834–5840.

[52] S. Kundu, M. Mandal, S. K. Ghosh, T. Pal, *Journal of Colloid and Interface Science* **2004**, *272*, 134 – 144.

[53] D. L. Stokes, J. P. Alarie, V. Ananthanarayanan, T. Vo-Dinh, *Proc. SPIE* **1999**, *3534*, 647–654.

[54] M. Fan, G. F. S. Andrade, A. G. Brolo, *Analytica Chimica Acta* **2011**, *693*, 7–25.

[55] B. Wiley, Y. Sun, B. Mayers, Y. Xia, *Chemistry – A European Journal* **2005**, *11*, 454–463.

[56] Haohao Lin, Jack Mock, David Smith, Ting Gao, M. J. Sailor, *The Journal of Physical Chemistry B* **2004**, *108*, 11654–11659.

[57] C. Fang, A. Agarwal, H. Ji, W. Y. Karen, L. Yobas, *Nanotechnology* **2009**, *20*, 405604.

[58] Xiaoling Li, Weiqing Xu, Junhu Zhang, Huiying Jia, Bai Yang, Bing Zhao, Bofu Li, Y. Ozaki, *Langmuir* **2004**, *20*, 1298–1304.

[59] N. E. Cant, K. Critchley, H.-L. Zhang, S. D. Evans, *Thin Solid Films* **2003**, *426*, 31–39.

[60] M. Oćwieja, Z. Adamczyk, K. Kubiak, *Journal of Colloid and Interface Science* **2012**, *376*, 1 – 11.

[61] M. Oćwieja, Z. Adamczyk, M. Morga, A. Michna, *Journal of Colloid and Interface Science* **2011**, *364*, 39 – 48.

[62] J. K. Daniels, and G. Chumanov, *The Journal of Physical Chemistry B* **2005**, *109*, 17936–17942.

[63] H.-W. Cheng, S.-Y. Huan, H.-L. Wu, G.-L. Shen, R.-Q. Yu, *Analytical Chemistry* **2009**, *81*, 9902–9912.

[64] Yugang Sun, Brian Mayers, Thurston Herricks, and Y. Xia, *Nano Letters* **2003**, *3*, 955–960.

[65] Y. Qin, X. Ji, J. Jing, H. Liu, H. Wu, W. Yang, *Colloids and Surfaces A: Physicochemical and Engineering Aspects* **2010**, *372*, 172–176.

[66] N. G. Bastús, F. Merkoçi, J. Piella, V. Puntes, *Chemistry of Materials* **2014**, *26*, 2836–2846.

[67] N. Pazos-Perez, W. Ni, A. Schweikart, R. A. Alvarez-Puebla, A. Fery, L. M. Liz-Marzan, *Chemical Science* **2010**, *1*, 174–178.

[68] M. A. Mahmoud, C. E. Tabor, M. A. El-Sayed, *The Journal of Physical Chemistry C* **2009**, *113*, 5493–5501.

[69] V. Santhanam, and R. P. Andres, *Nano Letters* **2004**, *4*, 41–44.

[70] Q. Yu, P. Guan, D. Qin, G. Golden, P. M. Wallace, *Nano Letters* **2008**, *8*, 1923–1928.

[71] Alexandre G. Brolo, Reuven Gordon, Brian Leathem, K. L. Kavanagh, *Langmuir* **2004**, *20*, 4813–4815.

[72] B. Yan, A. Thubagere, W. R. Premasiri, L. D. Ziegler, L. D. Negro, B. M. Reinhard, *ACS Nano* **2009**, *3*, 1190–1202.

[73] M. Kahl, E. Voges, S. Kostrewa, C. Viets, W. Hill, *Sensors and Actuators B: Chemical* **1998**, *51*, 285–291.

[74] J.-L. Yao, J. Tang, D.-Y. Wu, D.-M. Sun, K.-H. Xue, B. Ren, B.-W. Mao, Z.-Q. Tian, *Surface Science* **2002**, *514*, 108–116.

[75] Amanda J. Haes, Jing Zhao, Shengli Zou, Christopher S. Own, Laurence D. Marks, George C. Schatz, R. P. V. Duyne, *The Journal of Physical Chemistry B* **2005**, *109*, 11158–11162.

[76] M. J. Natan, *Faraday Discussions* **2006**, *132*, 321–328.

[77] Y. Yang, J. Shi, T. Tanaka, M. Nogami, *Langmuir* **2007**, *23*, 12042–12047.

[78] A. Kaminska, O. Inya-Agha, R. J. Forster, T. E. Keyes, *Physical Chemistry Chemical Physics* **2008**, *10*, 4172–4180.

[79] Andrea Tao, Franklin Kim, Christian Hess, Joshua Goldberger, Rongrui He, Yugang Sun, Younan Xia, and P. Yang, *Nano Letters* **2003**, *3*, 1229–1233.

[80] J. Theiss, P. Pavaskar, P. M. Echternach, R. E. Muller, S. B. Cronin, *Nano Letters* **2010**, *10*, 2749–2754.

[81] Y. Du, L. Shi, T. He, X. Sun, Y. Mo, *Applied Surface Science* **2008**, *255*, 1901 – 1905.

[82] K. Aslan, P. Holley, C. D. Geddes, *Journal of Materials Chemistry* **2006**, *16*, 2846–2852.

[83] F. Jäckel, J. Feldmann, in *Complex-Shaped Metal Nanoparticles*, Wiley, **2012**, pp. 429–454.

[84] R. G. Freeman, K. C. Grabar, K. J. Allison, R. M. Bright, J. A. Davis, A. P. Guthrie, M. B. Hommer, M. A. Jackson, P. C. Smith, D. G. Walter, et al., *Science* **1995**, *267*, 1629–

1632.

[85] M. S. Schmidt, J. Hübner, A. Boisen, *Advanced Materials* **2012**, *24*, OP11–OP18.

[86] E. C. Le Ru, P. G. Etchegoin, M. Meyer, *The Journal of Chemical Physics* **2006**, *125*, 204701.

[87] M. Rycenga, X. Xia, C. H. Moran, F. Zhou, D. Qin, Z.-Y. Li, Y. Xia, *Angewandte Chemie* **2011**, *123*, 5587–5591.

[88] J. A. Howarter, J. P. Youngblood, *Langmuir* **2006**, *22*, 11142–11147.

[89] Wolfgang Haiss, N. T. K. Thanh, J. Aveyard, D. G. Fernig, *Analytical Chemistry* **2007**, *79*, 4215–4221.

[90] M. Rycenga, P. H. C. Camargo, W. Li, C. H. Moran, Y. Xia, *The Journal of Physical Chemistry Letters* **2010**, *1*, 696–703.

[91] S.-H. Park, J.-H. Im, J.-W. Im, B.-H. Chun, J.-H. Kim, *Microchemical Journal* **1999**, *63*, 71 – 91.

[92] M. Oćwieja, M. Morga, Z. Adamczyk, *Journal of Nanoparticle Research* **2013**, *15*, 1–14.

[93] Katherine C. Grabar, Patrick C. Smith, Michael D. Musick, Jennifer A. Davis, Daniel G. Walter, Michael A. Jackson, Andrea P. Guthrie, and M. J. Natan, *Journal of the American Chemical Society* **1996**, *118*, 1148–1153.

[94] D. Pristinski, S. Tan, M. Erol, H. Du, S. Sukhishvili, *Journal of Raman Spectroscopy* **2006**, *37*, 762–770.

[95] P. Pinkhasova, H. Chen, M. W. G. M. (Tiny) Verhoeven, S. Sukhishvili, H. Du, *RSC Advances* **2013**, *3*, 17954–17961.

[96] S. L. Kleinman, R. R. Frontiera, A.-I. Henry, J. A. Dieringer, R. P. Van Duyne, *Physical Chemistry Chemical Physics* **2013**, *15*, 21–36.

[97] Y. Xia, Y. Xiong, B. Lim, S. E. Skrabalak, *Angewandte Chemie International Edition* **2009**, *48*, 60–103.

[98] M. Tejamaya, I. Römer, R. C. Merrifield, J. R. Lead, *Environmental Science & Technology* **2012**, *46*, 7011–7017.

[99] K. A. Huynh, K. L. Chen, *Environmental Science & Technology* **2011**, *45*, 5564–5571.

[100] A. Gopinath, S. V. Boriskina, W. R. Premasiri, L. Ziegler, B. M. Reinhard, L. D. Negro, *Nano Letters* **2009**, *9*, 3922–3929.

[101] P. Peng, A. Hu, Y. Zhou, *Applied Physics A* **2012**, *108*, 685–691.

[102] LinLin Zhao, K. Lance Kelly, and G. C. Schatz, *The Journal of Physical Chemistry B* **2003**, *107*, 7343–7350.

[103] A. M. E. Badawy, T. P. Luxton, R. G. Silva, K. G. Scheckel, M. T. Suidan, T. M. Tolaymat, *Environmental Science & Technology* **2010**, *44*, 1260–1266.